Imaging and quantifying the chemical communication between single particles in metal alloy

Louis Godeffroy, Aleksei Makogon, Sarra Gam Derouich, Frédéric Kanoufi*, Viacheslav Shkirskiy*

Université Paris Cité, ITODYS, CNRS, 75013 Paris, France

Abstract

The communication within particle agglomerates in industrial alloys can have significant impact on the macroscopic reactivity, putting a high demand on the adaptation of wide-field methodologies to clarify this phenomenon. In this work, we report the application of correlated optical microscopies probing *operando* both local pH and local surface chemical transformation correlated with identical location scanning electron microscopy to quantify *in-situ* the structure-reactivity of particle agglomerates of foreign elements in Al alloy. The optical operando analyses allow (i) to reveal and quantify the local production of OH^- from proton and oxygen reduction at individual Si- or Fe-rich microparticles and (ii) to quantify (and model) the chemical communication between these active sites, within a few µm range, on the local chemical transformation of the material. Wide-field image analysis highlights the statistical importance of the chemical communication that may introduce a new conceptual framework for the understanding the mechanisms in related fields of charge transfer, electrocatalysis and corrosion.

Keywords: Chemical communication, Optical microscopy, Correlative microscopy, Local electrochemistry, Alloy

Corresponding authors: frederic.kanoufi@univ-paris-diderot.fr, viacheslav.shkirskiy@cnrs.fr

Introduction

Industrially relevant metal interfaces are often structured at micro and nanoscales as they are composed of (sub)microparticles of diverse chemical composition embedded into a metal matrix.[1,2] Under operating conditions, these particles serve as centers of local electrochemical activities and define the macroscopic material's properties. It is often assumed that the averaged activities over individual particles define the macroscale material's response, implying that within the locally probed cluster each particle acts independently.[3,4] However, in more and more recent cases, the electrochemical activities of individual particles do not match the averaged or macroscopic response.[4–7] These examples highlight that individual particles can also interact with their neighbors, a phenomenon known as crosstalk or cooperative communication, of chemical and/or electrical origin. For example, in heterogeneous systems, cooperative chemical communication, can be established in a solution via overlapping of diffusion fields of species (as shown in a recent example between Pd and Au nanoparticles),[5] as well as on a surface (via spillover effects in catalysis).[8] Corroding metal interfaces are another example of heterogeneous systems where communication can occur.[7,9–13] The origin of this communication emerges from the dissimilar metals composing the alloy being in electrical contact with each other, forming myriads of local galvanic cells and sites of local degradation.[14,15] Having a high social impact, industrially relevant metal alloys also offer a wealth of complexity due to a wide range of size or compositional distribution of particles.[16] Industrial Al alloys are the typical example of such complex system that is considered in this work.

A few studies on industrial Al2024 alloy suspected the presence of cooperative communication around dense particle clusters, visible from the appearance of rings of corrosion products.[7,9–13] It was further hypothesized that the crosstalk manifests through overlapping of OH^- fluxes generated on the surface of individual particles, creating complex patterns of local pH distribution.[9,10] Some authors suggested that the crosstalk in particle clusters can be responsible for the low consistency of corrosion tests for Al alloys, highlighting a high practical importance and the necessity of developing tools for the detailed quantification of particle communication.[12]

The *in-situ* diagnosis of such situation and the screening of the crosstalk remains a challenging experimental task, because, unless under forced corrosion, no current is exchanged with an external device. It is worth mentioning that recently developed high resolution local electrochemical strategies offer tremendous capabilities in the structure-function characterization at the true nm size.[17–20] In particular, nanopipet methods have emerged as a

robust and versatile toolbox for single entity characterization in the fields of biology,[21] electrocatalysis,[22] batteries[23] and corrosion[24,25] to name only a few. Despite their great success, these strategies belong to the family of scanning methods and at their best, will always be limited in a time domain imposed by the physical displacement of the probe between active sites.[26] This is a crucial limitation as in principle, the crosstalk can interconnect active sites 10s-100s of μm away, instantaneously and dynamically, manifesting itself through nanoscopic solid conversion.[11,13] Therefore, the development of wide field highly resolved methods are required, among which optical methods are proved to be the most prominent to probe *operando* wide range of chemical processes in electrochemical energy-related systems.[27–29]

In the present work, we use correlated fluorescence microscopy[30,31] and reflection-based optical microscopy (RM)[32,33] to address these challenges and provide the direct measurement of chemical crosstalk communication between particles on the example Al6061 alloy. RM is a label free optical imaging technique relying on local changes in the refractive index of the imaged surface. Therefore, it is highly sensitive to various chemical phase conversion.[27,29,34,35] Reflection-based optical microscopy are particularly appealing for their ability to image local fluxes of chemical species from local detection of refractive index variations, illustrated from the pioneering detection of local gas electrogeneration at nanocatalysts[36] to more recent imaging of flux of Li^+ ions within individual microparticles during a battery electrode material dis/charge.[37,38] In contrast to RM, fluorescence microscopy relies on the use of a fluorescent probe sensitive to the formation of specific products which has enabled imaging different electrochemical reaction.[31,39] Herein, we combined the unique advantages of these two approaches as illustrated in Fig. 1a and correlate them to *ex-situ* identical location structural identification of the particles within the alloy. We used the pH-dependency of fluorescence emission of fluorescein isothiocyanate (FITC) to map the distribution of local OH^- production. On the other hand, the reflection imaging is used to evaluate the local conversion of the surface coating over Fe- and Si-rich particle clusters embedded in an Al matrix of Al6061 alloy. In this way, the holistic picture of localized electrochemical processes is provided. The conversion is studied during the first minutes of immersion of a polished Al6061 alloy sample surface in a slightly acidic environment. Underpinned by complementary numerical analysis using finite element method (FEM) modeling and correlated scanning electron microscopy, this work rises the importance of investigating the inter particle communication for better understanding of macroscopic material reactivity.

Experimental

Correlative microscopy approach

Detailed experimental conditions are provided in supplementary information (SI-1). Briefly (Fig. 1), fluorescence imaging was carried out on an inverted epifluorescence microscope (Olympus IC71) equipped with a ×40 0.6-NA air objective (Olympus LUMPlanFL N). The sample was illuminated with a white light source (Hg lamp) coupled through Olympus U-MSWB2 cube (with excitation filter within 450-480 nm and emission at 500 nm) to excite and reveal fluorescence emitted from the deprotonated FITC probe (*ca.* 0.2 mM), occurring for pH higher than *ca.* 6 (Fig. S1).[40] A digital USB color camera (UI-3080CP Rev. 2, IDS with CMOS 2456×2054-pixel detector) collected the fluorescence emitted from the solution. FL images covering a wide field of 288 × 288 μm^2 were recorded at a speed of 2 frames per second (fps) with 500 ms accumulation time.

RM imaging was carried out an Olympus microscope, equipped with a water immersion objective (magnification ×60 1.00-NA (Olympus LUMPlanFL N)) with a focus distance of *ca.* 3 mm and a MV-D1024-160-CL-12 CCD camera (Photonfocus, 1024×1024 pixels, 14 bit). A halogen white lamp, filtered in the blue at 490 nm with an interference filter (spectral bandwidth of 20 nm), served as the light source. Each acquired image, corresponding to 184x184 μm^2 wide field, consisted of a stack of 4 snapshots, each integrated over 50 ms, for a total duration of 200 ms. All reflectivity maps were normalized by the intensities from the first reflectivity image and converted to the change of the thickness of surface films according to the Fresnel model described in SI-1.

Identical locations from fluorescence and RM imaging were analyzed with scanning electron microscopy (SEM) and energy-dispersive X-ray spectroscopy (EDX) before and after the optical experiments. The original images, in conjunction with examples of Python scripts illustrating the processing methodologies, are accessible in the Zenodo repository (https://doi.org/10.5281/zenodo.7963186). These resources are provided under the terms of a Creative Commons Attribution 4.0 International license.

The FEM model was built in a 3D geometry with COMSOL Multiphysics 5.5 software (1) to simulate the steady-state pH distribution and (2) to simulate the transients of $Al(OH)_3$ dissolution/precipitation in the case of galvanic coupling of Fe- and Si-rich particles dispersed in Al matrix observed optically for Al6061 alloy (details in SI-2).

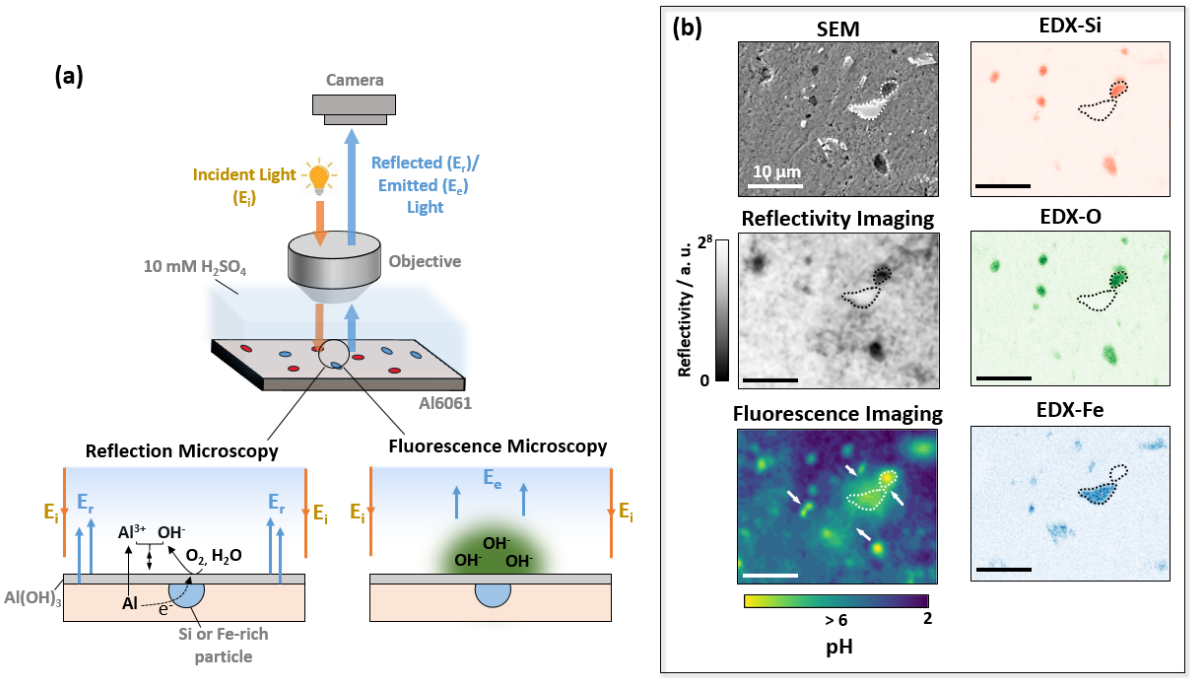

Fig. 1 *Correlative multimicroscopy approach. (a) Scheme of the setup for correlative operando observations with RM and fluorescence microscopy of the mirror polished Al6061 interface (< 40 nm roughness, SI-3) exposed to 10 mM H_2SO_4. Bottom left: diagram of the optical signal generation in RM during precipitation of $Al(OH)_3$ surface films induced by galvanic coupling between cathodically active particle embedded into anodically active Al matrix. Incident light (E_i) filtered at 475 nm is focused on the metal surface. The collected light includes the contributions of reflected light (E_r) from the surfaces of oxide/hydroxide film and the metal. Their interference lies the foundation for the quantification of local surface thickness changes via the Fresnel equations. Bottom right: optical signal generation in fluorescence microscopy during OH^- generation over single particles. E_i filtered at 450-480 nm is focused on the metal interface exposed to 10 mM H_2SO_4 solution saturated with a fluorescein molecule. When the local pH over overpasses ca. 6, the fluorescein probe deprotonates and emits the light (E_e) collected with a system of filters at 500 nm.*[40] *Details on optical configurations can be found in SI-1. (b) Identical location images over a zoomed region of interest (wider optical field of view presented in Fig. 4) of an Al6061 interface: ex-situ secondary electron SEM, EDX maps of Si, O and Fe distribution and operando reflectivity and fluorescence imaging. The particle shapes of one Fe-rich and one Si-rich particles are outlined for visual reference. Arrows on the fluorescence image show cases of overlapping of OH^- diffusion fields generated in neighboring particles, called herein chemical communication. The scale bars are 10 µm.*

Results and Discussion

Distribution of pH over particle clusters

The investigation of inter-particle chemical communication was performed in a correlative multimicroscopy approach (Fig. 1, see also SI-1 for experimental details). The surface of the mirror polished Al6061 sample was firstly analyzed with SEM and EDX, then placed in a corrosive 10 mM H_2SO_4 electrolyte (estimated pH of 1.87) in the optical setup (Fig. 1a). Wide field optical images (110×170 μm²) have been recorded either under white light illumination (reflectivity) or in the presence of a fluorophore for fluorescence analysis. White light reflectivity images of the sample show (see Fig. 4 and related SI-7 for the wide field image and zoom over a selected region of interest in Fig.1b) the presence of contrasted features which will be later identified as region of interest identical to SEM-EDX *ex-situ* images. The presence of FITC in the corrosive electrolyte allows, by switching to the fluorescence imaging mode (*ca.* 2 min after the contact electrolyte/sample contact), to reveal the local alkalinization of the sample/solution interface: once pH locally overpasses the value of *ca.* 6, the bright green fluorescence emission of the deprotonated FITC is detected.[40] It should be noted that theoretically, the presence of FITC could influence the reactivity of the Al alloy. However, existing literature on the Al2024 alloy,[41] as well as observations of crosstalk both with and without FITC in the current study, suggest that such an impact is likely to be minimal.

The *ex-situ* SEM analysis shows that there are two types of particles identified from secondary electron images with bright and dark contrast (Fig. 1b). EDX analysis (SI-4) complemented with XRD characterization of bulk Al6061 composition (SI-5) revealed that particles with the dark contrast are SiO_2 phase (or simply Si-rich) and the particles with bright contrast are Al_3Fe phase (or Fe-rich). RM microscopy also reveals the presence of these particles as regions of lower reflectivity than the surrounding Al matrix (Fig. 1b): SiO_2 particles appear as dark spots while Al_3Fe particles are shown as grey areas, nearly indistinguishable in contrast to the dark SiO_2 regions but clearly visible on 2D profiles (SI-6). The fluorescence image at identical location (Fig. 1b) exhibits diffusive spots of green lights around all particles while there is no light emission over the Al matrix. This is a direct evidence of pH increase over SiO_2 and Al_3Fe particles, which according to the literature, are polarized cathodically relative to Al matrix and serve as the center of local proton and oxygen reductions.[42–44] Remarkably, the fluorescence image also provides evidence of overlapping of OH^- diffusion fields, suggesting a chemical communication of OH^- fluxes between neighboring particles.

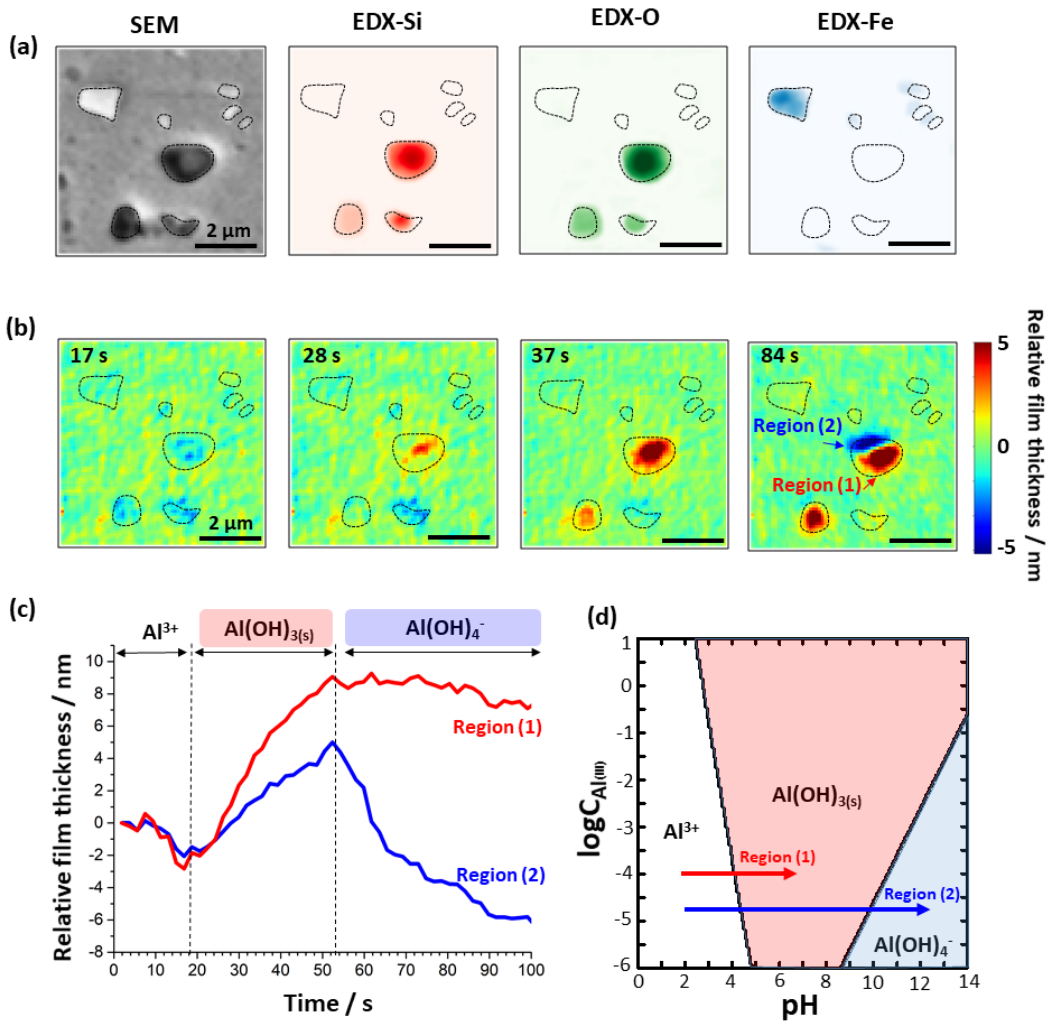

Fig. 2 *Dynamics of chemical communication surveyed with RM. (a) SEM-EDX analysis of surface inspected with RM, showing the distribution of particles and their chemical composition. (b) Evolution of the relative film thickness at 17, 28, 37 and 84 s exposure to 10 mM* H_2SO_4*. The whole collection of frames is in Movie S2. The scale bars are 2 µm. (c) The evolution of relative film thickness averaged over red (region 1) and blue (region 2) zones over the particle in the center at 84 s. Inferred regions of stability of Al(III) species are mentioned on the top. (d) Diagram of Al(III) stability as a function of pH calculated in Hydro-Meduza software*[45] *(soluble species taken into account:* Al^{3+}*,* $Al(OH)_2^+$*,* $Al(OH)_3$*,* $Al(OH)_4^-$*,* $Al_{13}O_4(OH)_{24}^{7+}$*,*$Al_2(OH)_2^{4+}$*,* $Al_3(OH)_4^{5+}$*,* $AlOH^{2+}$*; solid species:* $Al(OH)_3(s)$*,* $AlOOH(s)$*,* $Al_2O_3(s)$*).*

Localized transformation of surface films over particle clusters

The as-prepared Al6061 interface was shown to be covered by a 10 nm layer of Al_2O_3, $Al(OH)_3$ and AlOOH species (SI-1).[46,47] For the sake of simplicity we mention only the thermodynamically stable $Al(OH)_3$ phase[45] in the graphics and further discussions. The *in-situ* transformation of this pre-formed $Al(OH)_3$ layer is elucidated from the dynamic mono-wavelength (λ=490nm) optical RM monitoring of the surface reflectivity while exposed to 10 mM H_2SO_4 with reflectivity images taken at 0.5 Hz acquisition rate during *ca.* 3 min (details in SI-1). The change of the intensities of the reflected light from raw images are related to the transformation of the preformed $Al(OH)_3$ surface films. In a first approximation, an optical model based on Fresnel equations (details in SI-1) can be used to deduce, from the raw images, maps of relative $Al(OH)_3$ thickness over the surface as presented in Fig. 2b. Note that in this section, we focus on a small region of 7.5×7.5 μm^2 presented in Fig. 2a containing a few Fe- and Si-rich particles. The discussion on the full wide-field imaged surface, 110×170 μm^2 showing > 1000 particles is provided section 3.4. Fig. 2b presents several selected maps of the Al interface during dynamic change for times up to 84 s where the most drastic changes are visible. The values of the surface film thickness are relative to t = 0 s when H_2SO_4 was added. The whole sequence of images recorded over the full field of view was reconstructed into the movie and is available in Movie S1.

The most remarkable observation in Fig. 2b is that every Si-rich particle shows a unique pattern of evolution of the relative oxide film thickness, visible from different color changes over timeframes. After the initial decrease over all Si-rich particles (visible from the blue color at 17 s), the film thickness abruptly increases over the particle at the left bottom corner (depicted in red at 37 s and 84 s), whereas only a slight increase in the film thickness is observed over the particle at the bottom center (becoming greener at 37 s and yellow at 84 s). A possible explanation for this is that the activity levels of individual particles can differ. The most striking (and likely unexpected) behavior is detected at the particle present in the center of the image. If the film thickness initially increases homogeneously over its whole surface (becoming yellow/red at 28 s and 37 s), in the last frame a region of strong decrease in film thickness appears in the top corner of this central particle (visible from the blue color at 84 s). To highlight these noteworthy local effects, the average values of the film thickness evolution over the two regions of distinct activities of the central particle (named regions (1) and (2) in Fig. 2b) are plotted as a function of time in Fig. 2c for a detailed analysis.

An initial film dissolution is observed in both regions in Fig. 2c, continuing to up to 18 s. It can be explained by the initial low solution pH enabling the solubilization of Al(III) as it

is thermodynamically stable in solution according to the Al(III)-pH diagram given in Fig. 2d. Then, the local pH should increase due to the release of OH^- from cathodic processes on particle surface, causing the precipitation of $Al(OH)_3$. It explains the increased film thickness between 18 s and 53 s. The sudden decrease in film thickness over region (2) after 53 s suggests a redissolution of the film. This situation at alkaline pH can be explained if the pH increase above 10 which would lead to the formation of $Al(OH)_4^-$ soluble species. Schematically, the behavior of both regions could be rationalized by a pH change along the trajectories depicted on the Al(III)-pH diagram following the arrows depicted in Fig. 2d. Therefore, the optical observations, rationalized according to the pH diagram of Al(III) species stability, suggest a strong local pH gradient over the surface of this single Si-rich particle, caused by the superposition of OH^- fields from individual particles as observed in fluorescence image Fig. 1b. The FITC fluorescence mapping in Fig. 1 depicts regions of pH > 6-7, suggesting the local conversion of ca. 20 mM H^+ from the 10 mM H_2SO_4 solution. Noteworthy, the reach of pH 10 region requires only a supplemental 0.1mM OH^- production which is possible owing to the presence of O_2 within the solution.

Differently, the film thickness does not change over any of the Fe-rich particles during exposure to 10 mM H_2SO_4 (Fig. 2b). On the one hand, surface films over Fe-rich particles can be composed of Fe oxides/hydroxides, which are stable in basic pH and will only dissolve in extremely basic conditions (pH > 14).[48] On the other hand, Fe-rich phases also serve as local cathodes (Fig. 1b) and therefore, the release of Fe ions seems to be significantly suppressed as well as the growth of Fe-rich films. The chemical communication between these Fe-rich particles and central Si-rich particle, via superposition of localized OH^- fluxes, is rationalized in detail below with the aid of FEM modelling.

Numerical simulations of the particle chemical communication

Two types of galvanically coupled electrochemical reactions were considered (Fig. 3a, left): anodic Al dissolution that produces Al^{3+} ions and cathodic oxygen reduction and hydrogen evolution that produces OH^-. The distribution of cathodic and anodic areas (Fig. 3a, left) was chosen to mimic the particle positions observed in *in-situ* RM experiment: the Si-rich particle is represented by a 2 μm in diameter disk, while the three Fe-rich particles are represented by 1 μm in diameter disks located on the same side relative to the Si-rich particle. The pH of solution was set to 2.0 (close to theoretical pH value of 1.87 in 10 mM H_2SO_4). Further details about simulations can be found in SI-2.

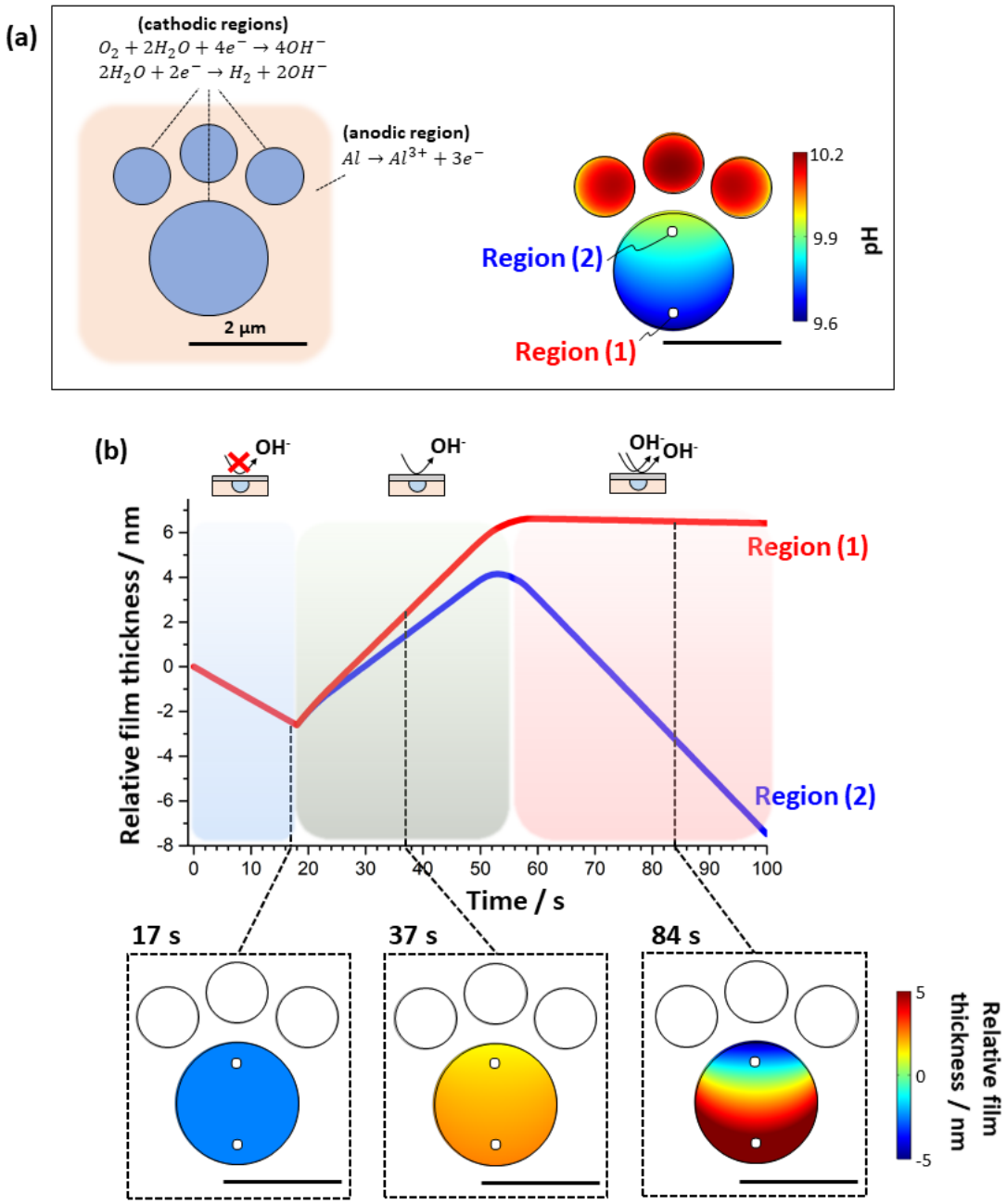

Fig. 3 *Overview of FEM simulations. (a) Left, size and position of the cathodic and anodic regions with a brief summary of electrochemical reactions considered. Right, steady-state pH distribution over cathodic zones, showing the pH gradient over the largest cathodic region. Regions 1 and 2 are highlighted in analogy to those chosen from the experimental observations in Fig. 2. (b) Top, evolution of relative film thickness in regions 1 and 2. The schemes on top of the film thickness evolution depict the activity of the cathodic particles in each regime. Bottom, the spatial distribution of the relative film thickness over the large cathodic region after 17, 37 and 84 s of simulations. The scale bars are 2 µm.*

Note that we do not aim to reproduce the exact conditions (particle sizes and positions) since, in any case, other parameters (local potential and current distributions) were not accessible experimentally. Opposed to that, we use simulations to only illustrate the underlying physical principles that can explain this apparently unexpected distribution of precipitation kinetics of surface films over a Si-rich particle.

A first set of simulations was carried out under steady-state conditions without considering the processes of precipitation/dissolution of $Al(OH)_3$ in order to examine the extent of pH distribution solely related to the OH^- generation from the cathodic zones. Fig. 3a (right) shows that overlapping of diffusion fields of OH^- results in pH gradients over the particles. This is most visible from the pH distribution over the large particle where the pH varies from *ca.* 10.0 to 9.6 as we move away from the smaller particles. This pH gradient is an illustration of the chemical communication between neighboring particles that can manifest itself in the different precipitation kinetics over the particle.

The precipitation/dissolution processes of $Al(OH)_3$ were then added into the simulation now run in transient mode. The kinetic parameters of $Al(OH)_3$ film transformation and of the cathodic activity over the particle were chosen (within the reported in literature values) to fit the experimental evolution over the Si-rich particle (SI-2, Table S2-1). The evolution of the relative film thickness in regions (1) and (2) as well as the distributions of relative film thickness at different times over the large particle are shown in Fig. 3b.

In the first period between 0 s and 18 s, the cathodic sites were considered as inactive, suggesting they are strongly inhibited by an initial oxide layer. Therefore, the pH distribution was homogenous and close to that of the bulk pH value. This leads to the homogeneous dissolution of the $Al(OH)_3$ film over the metal and particles. At the beginning of the second period between 18 s and 58 s, the cathodic activity was then considered. The kinetics of cathodic reactions was adjusted to match the precipitation kinetics observed experimentally. Finally, in the last period starting at 58 s, the cathodic activity was set to a higher value corresponding to that used in the steady-state simulations, which results in a nearly steady film thickness in region (1) and the dissolution of surface films in region (2) of the large particle.

Simulated curves of the surface film transformation (Fig. 3b, top) are in a good agreement with the experimental data (Fig. 2b), reinforcing hypothesis of the chemical communication between Fe-rich and Si-rich particles. Thus, the essential conditions for chemical communication necessitate the presence of neighboring particles and their agglomeration on only one side in relation to the central particles. In the subsequent section,

we will delve into wide-field RM observations, offering additional examples of chemical communication to further elaborate on these aspects.

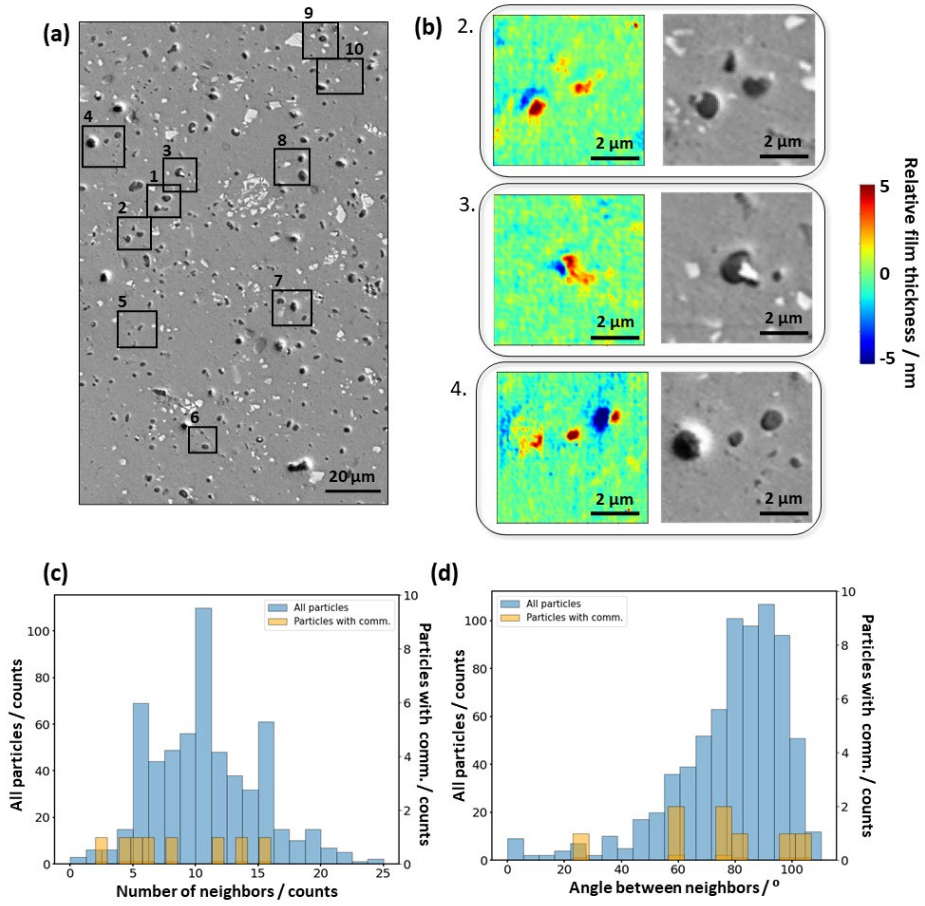

Fig. 4 *Overview of the examples of chemical communication. (a) SEM image of the entire surface analyzed in a wide field of 110×170 µm² during RM observations. The marked areas indicate where chemical communication was detected with area 1 described in detail in the previous section in Fig. 2. (b) Additional examples of chemical communication in areas 2, 3, and 4. All optical images of the chemical communication are available in SI-7 and SI-8. The image on the left shows relative film thickness (obtained in-situ), and the image on the right shows the identical location SEM image (obtained ex-situ) during exposure to 10 mM H_2SO_4. (c) Histogram depicting the number of neighboring particles within a 10 µm radius surrounding all particles, as well as those exhibiting chemical communication. (d) Histogram depicting the standard deviation of angle between neighboring particles within a 10 µm radius surrounding all particles, as well as those exhibiting chemical communication.*

Particle distribution in the examples of chemical communication

The comprehensive wide-field image (110×170 µm²) showcases 10 instances of chemical communication, all identified in Fig. 4a on the SEM image, with a few examples from optical images in Fig. 4b and additional instances provided in SI-7 and SI-8. The chemical

communication was identified through visual identification of particles displaying both dissolution and precipitation patterns based on optical observations. The chemical communication covers *ca.* 20 % of the analyzed interface and stresses the prevalence of chemical communication on Al alloy interfaces. The entire sequence of optical images captured over the full field of view has been reconstructed into a movie, available in Movie S2. As in the previously described example, chemical communication in regions 2, 3, and 4 (Fig. 3b) is evident from the asymmetric patterns of relative film thickness. In cases 2-4, particles exhibiting chemical communication are surrounded by other particles (visible in SEM images in Fig. 3b), and these neighboring particles appear to be preferentially situated on one side, aligning with the FEM model that explains chemical communication as the overlapping of diffusion fields of produced OH^- ions on neighboring particles. To rigorously analyze the influence of these two parameters, we counted the number of neighbors and the angle between them, and plotted the data in histogram form in Fig. 4c and d, respectively. We limited our analysis to the closest neighbors situated less than 10 μm from the particle of interest, as the contribution of particles farther away should be negligible (as observed from FEM simulations in Fig. 3). Additionally, we excluded examples 4 and 9 from the histograms, as these areas are in close proximity to the border of observation, and some neighboring particles may be outside the analysis zone.

Fig. 4c illustrates that particles exhibiting chemical communication are consistently surrounded by neighboring particles, with counts ranging from 3 to 16. The distribution of the number of neighbors for all particles adheres to a Gaussian distribution, with a peak occurring at 9-12 neighboring particles. This suggests that the particles are densely packed on the Al interface. The standard deviation of the angle between neighbors provides information about the preferential positioning of neighbors in relation to the particle of interest. When the angle is close to 0°, neighbors are situated predominantly on one side, while an increase in the angle up to approximately 100° results in a more homogeneous dispersion of neighbors. The angle between particles exhibiting chemical communication varies widely, ranging from 20° to 100°, which implies that some neighbors are inclined to be positioned on one side of the particle of interest, while others are more evenly dispersed. The general trend for all particles peaks at 60-100°, indicating that, on average, neighbors have a slight tendency to cluster on one side of individual particles.

In summary, the histogram analysis reveals that particles with chemical communication do not exhibit any specific trends in terms of their neighbors' distribution when compared to the overall tendencies. A plausible explanation for this could be that individual particles have

varying activities, and thus, apart from their position, their individual contributions should be also considered. It is also important to note that the transition between different dissolution/precipitation kinetic regimes in numerical simulations (Fig. 3) was defined using an empirical parameter related to the inhibition of cathodic sites, which is also connected to the activities of individual particles. Existing literature suggests that factors such as thickness, composition, and structure of dynamically evolving surface films can influence the kinetics of cathodic reactions.[49–51] In light of this, direct in-situ measurements of local electrochemical activity are necessary to complement the in-situ observation of surface deposition/dissolution and to rigorously develop a physical model for chemical communication. An intriguing direction for future research would be to investigate the use of local complementary probing techniques, such as nanopipet methods in a combined opto-electrochemical approach,[52–55] to supplement optical observations with direct local electrochemical measurements.

Conclusions

The pH variations and accompanied transformation kinetics of surface films at the nanoscale on Al6061 alloy in 10 mM H_2SO_4 was investigated around Fe- and Si-rich micrometric particles using *in-situ* fluorescence and reflection-based optical microscopy in combination with *ex-situ* SEM-EDX surface characterization. In contrast to the surface films over Fe-rich particles where no significant changes were observed, the thickness of the surface films over Si-rich particles dynamically evolved over time. The reactivity over each Si-rich particle could be monitored with sub-micrometric spatial resolution. It demonstrated a unique pattern, presumably defined by the position of surrounding particles. In particular, we have shown with fluorescence imaging and numerical simulations that the presence of cathodically active small particles nearby a large particle can generate a sufficient pH gradient over the large particle to result in the simultaneous precipitation on one side and dissolution of the surface films on the other side of the large Si-rich particle. This phenomenon, coined as a chemical communication, was observed experimentally on Si-rich particles, and particularly those located near Fe-rich particles. Further observations indicated that the spatial configuration of adjacent particles is not the sole determinant of the observed pattern. Thus, differential local reactivities across individual particles would likely exert a significant impact. The wide-field reflective image showed that a significant part (*ca.* 20 %) of the observed interface is subjected to chemical communication. Overall, the presence of chemical communication implies that the macroscopic reactivity of Al alloy interfaces is not simply defined by the sum of its individual entities but can be a result of the communication between them. This opens an interesting

avenue for future works on the detailed investigation of reactivities of particle assemblies and their impact on bulk material properties.

Supporting Information

The supporting information available: Experimental part (SI-1), FEM simulations of particle crosstalk (SI-2), Roughness of polished Al6061 sample (SI-3), Surface state (SI-4), Bulk material structure (SI-5), 2D profile of reflectivity image over Fe-rich particle (SI-6), Wide-field view of analyzed interface (SI-7), Summary of the crosstalk appearances in the wide-field image (SI-8).

Acknowledgements

This work was partially financially supported by the Agence Nationale de la Recherche (ANR) Jeunes chercheuses, jeunes chercheurs, ANR JCJC, program (OCTAWA project, ANR-22-CE29-0010-01). L.G. acknowledges the Ecole normale supérieure Paris-Saclay for funding. The authors acknowledge the ITODYS-LISA XRD facility, the ITODYS SEM-EDX facility, the Ile-de-France region, and initiative d'excellence (IDEX) program for financial support of the AFM-Beam-Rex platform. The authors also gratefully thank Sophie Nowak and Xiaonan Sun for discussions on the XRD data and implementation of AFM experiments.

References

(1) Birbilis, N.; Choudhary, S.; Scully, J. R.; Taheri, M. L. A Perspective on Corrosion of Multi-Principal Element Alloys. *npj Mater. Degrad.* **2021**, *5*, 14. https://doi.org/10.1038/s41529-021-00163-8.

(2) George, E. P.; Raabe, D.; Ritchie, R. O. High-Entropy Alloys. *Nat. Rev. Mater.* **2019**, *4* (8), 515–534. https://doi.org/10.1038/s41578-019-0121-4.

(3) Tao, B.; Daviddi, E.; Yule, L.; Bentley, C. L.; Unwin, P. Correlative Electrochemistry-Microscopy of Li-Ion (de)Intercalation at Series of Individual LiMn2O4 Particles. *Angew. Chemie Int. Ed.* **2019**, *26*, 4654–4659. https://doi.org/10.1002/anie.201814505.

(4) Daviddi, E.; Chen, Z.; Beam Massani, B.; Lee, J.; Bentley, C. L.; Unwin, P. R.; Ratcliff, E. L. Nanoscale Visualization and Multiscale Electrochemical Analysis of Conductive Polymer Electrodes. *ACS Nano* **2019**, *13* (11), 13271–13284. https://doi.org/10.1021/acsnano.9b06302.

(5) Zou, N.; Zhou, X.; Chen, G.; Andoy, N. M.; Jung, W.; Liu, G.; Chen, P. Cooperative Communication within and between Single Nanocatalysts. *Nat. Chem.* **2018**, *10* (6), 607–614. https://doi.org/10.1038/s41557-018-0022-y.

(6) Davies, T. J.; Compton, R. G. The Cyclic and Linear Sweep Voltammetry of Regular

and Random Arrays of Microdisc Electrodes: Theory. *J. Electroanal. Chem.* **2005**, *585* (1), 63–82. https://doi.org/10.1016/j.jelechem.2005.07.022.

(7) Jakab, M. A.; Little, D. A.; Scully, J. R. Experimental and Modeling Studies of the Oxygen Reduction Reaction on AA2024-T3. *J. Electrochem. Soc.* **2005**, *152* (8), B311–B320. https://doi.org/10.1149/1.1949047.

(8) Shen, T.; Wang, S.; Zhao, T.; Hu, Y.; Wang, D.; Shen, T.; Wang, S.; Zhao, T.; Hu, Y.; Wang, D. Recent Advances of Single-Atom-Alloy for Energy Electrocatalysis. *Adv. Energy Mater.* **2022**, *12* (39), 2201823. https://doi.org/10.1002/AENM.202201823.

(9) Hughes, A. E.; Boag, A.; Glenn, A. M.; McCulloch, D.; Muster, T. H.; Ryan, C.; Luo, C.; Zhou, X.; Thompson, G. E. Corrosion of AA2024-T3 Part II: Co-Operative Corrosion. *Corros. Sci.* **2011**, *53* (1), 27–39. https://doi.org/10.1016/j.corsci.2010.09.030.

(10) Hughes, A.; Muster, T. H.; Boag, A.; Glenn, A. M.; Luo, C.; Zhou, X.; Thompson, G. E.; McCulloch, D. Co-Operative Corrosion Phenomena. *Corros. Sci.* **2010**, *52* (3), 665–668. https://doi.org/10.1016/j.corsci.2009.10.021.

(11) Denissen, P. J.; Garcia, S. J. Reducing Subjectivity in EIS Interpretation of Corrosion and Corrosion Inhibition Processes by In-Situ Optical Analysis. *Electrochim. Acta* **2019**, *293*, 514–524. https://doi.org/10.1016/j.electacta.2018.10.018.

(12) Schneider, O.; Ilevbare, G. O.; Scully, J. R.; Kelly, R. G. In Situ Confocal Laser Scanning Microscopy of AA 2024-T3 Corrosion Metrology. II. Trench Formation around Particles. *J. Electrochem. Soc.* **2004**, *151* (8), B465. https://doi.org/10.1149/1.1764781.

(13) Denissen, P. J.; Homborg, A. M.; Garcia, S. J. Interpreting Electrochemical Noise and Monitoring Local Corrosion by Means of Highly Resolved Spatiotemporal Real-Time Optics. *J. Electrochem. Soc.* **2019**, *166* (11), C3275–C3283. https://doi.org/10.1149/2.0341911jes.

(14) Hayden, S. C.; Chisholm, C.; Eichmann, S. L.; Grudt, R.; Frankel, G. S.; Hanna, B.; Headrick, T.; Jungjohann, K. L. Genesis of Nanogalvanic Corrosion Revealed in Pearlitic Steel. *Nano Lett.* **2022**, *22*, 7087–7093. https://doi.org/https://doi.org/10.1021/acs.nanolett.2c02122.

(15) Kosari, A.; Zandbergen, H.; Tichelaar, F.; Visser, P.; Taheri, P.; Terryn, H.; Mol, J. M. C. In-Situ Nanoscopic Observations of Dealloying-Driven Local Corrosion from Surface Initiation to in-Depth Propagation. *Corros. Sci.* **2020**, *177*, 108912. https://doi.org/10.1016/J.CORSCI.2020.108912.

(16) Han, J.; Gharbi, O. Current State of Electrochemical Techniques and Corrosion Rate Analysis for Next-Generation Materials. *Curr. Opin. Electrochem.* **2022**, *36*, 101131. https://doi.org/10.1016/J.COELEC.2022.101131.

(17) Bentley, C. L.; Edmondson, J.; Meloni, G. N.; Perry, D.; Shkirskiy, V.; Unwin, P. R. Nanoscale Electrochemical Mapping. *Anal. Chem.* **2019**, *91* (1), 84–108. https://doi.org/10.1021/acs.analchem.8b05235.

(18) Bentley, C. L. Scanning Electrochemical Cell Microscopy for the Study of (Nano)Particle Electrochemistry: From the Sub-Particle to Ensemble Level. *Electrochem. Sci. Adv.* **2022**, *2* (3), e2100081. https://doi.org/10.1002/ELSA.202100081.

(19) Li, Y.; Morel, A.; Gallant, D.; Mauzeroll, J. Ag+Interference from Ag/AgCl Wire Quasi-Reference Counter Electrode Inducing Corrosion Potential Shift in an Oil-Immersed Scanning Micropipette Contact Method Measurement. *Anal. Chem.* **2021**, *93* (28), 9657–9662. https://doi.org/https://doi.org/10.1021/acs.analchem.1c01045.

(20) Wang, Y.; Li, M.; Gordon, E.; Ye, Z.; Ren, H. Nanoscale Colocalized Electrochemical and Structural Mapping of Metal Dissolution Reaction. *Anal. Chem.* **2022**, *94* (25), 9058–9064. https://doi.org/https://doi.org/10.1021/acs.analchem.2c01283.

(21) Zhu, C.; Huang, K.; Siepser, N. P.; Baker, L. A. Scanning Ion Conductance Microscopy. *Chem. Rev.* **2021**, *121* (19), 11726–11768. https://doi.org/10.1021/acs.chemrev.0c00962.

(22) Guo, S. X.; Bentley, C. L.; Kang, M.; Bond, A. M.; Unwin, P. R.; Zhang, J. Advanced Spatiotemporal Voltammetric Techniques for Kinetic Analysis and Active Site Determination in the Electrochemical Reduction of CO2. *Acc. Chem. Res.* **2022**, *55* (3), 241–251. https://doi.org/https://doi.org/10.1021/acs.accounts.1c00617.

(23) Martín-Yerga, D.; Milan, D. C.; Xu, X.; Fernández-Vidal, J.; Whalley, L.; Cowan, A. J.; Hardwick, L. J.; Unwin, P. R. Dynamics of Solid-Electrolyte Interphase Formation on Silicon Electrodes Revealed by Combinatorial Electrochemical Screening. *Angew. Chemie Int. Ed.* **2022**, *61* (34), e202207184. https://doi.org/10.1002/ANIE.202207184.

(24) Li, M.; Wang, Y.; Blount, B.; Gordon, E.; Muñoz-Castañeda, J. A.; Ye, Z.; Ren, H. Stochastic Local Breakdown of Oxide Film on Ni from Identical-Location Imaging: One Single Site at a Time. *Nano Lett.* **2022**, *22* (15), 6313–6319. https://doi.org/https://doi.org/10.1021/acs.nanolett.2c02018.

(25) Li, Y.; Morel, A.; Gallant, D.; Mauzeroll, J. Correlating Corrosion to Surface Grain Orientations of Polycrystalline Aluminum Alloy by Scanning Electrochemical Cell

Microscopy. *ACS Appl. Mater. Interfaces* **2022**, *14* (41), 47230–47236. https://doi.org/https://doi.org/10.1021/acsami.2c12813.

(26) Momotenko, D.; Byers, J. C.; McKelvey, K.; Kang, M.; Unwin, P. R. High-Speed Electrochemical Imaging. *ACS Nano* **2015**, *9* (9), 8942–8952. https://doi.org/10.1021/acsnano.5b02792.

(27) Lemineur, J.-F.; Wang, H.; Wang, W.; Kanoufi, F. Emerging Optical Microscopy Techniques for Electrochemistry. *Annu. Rev. Anal. Chem.* **2022**, *15* (1), 57–82. https://doi.org/10.1146/annurev-anchem-061020-015943.

(28) Chen, B.; Zhang, H.; Xuan, J.; Offer, G. J.; Wang, H. Seeing Is Believing: In Situ/Operando Optical Microscopy for Probing Electrochemical Energy Systems. *Adv. Mater. Technol.* **2020**, *5* (10), 2000555. https://doi.org/10.1002/admt.202000555.

(29) Kanoufi, F. Electrochemistry and Optical Microscopy. In *Encyclopedia of Electrochemistry*; Wiley, 2021. https://doi.org/https://doi.org/10.1002/9783527610426.bard030108.

(30) Gao, J.; Zhao, R.; Wang, Y.; Xie, R.-C.; Wang, W. Rapid Fluorescent Mapping of Electrochemically Induced Local PH Changes. *Adv. Sens. Energy Mater.* **2022**, *1* (4), 100030. https://doi.org/10.1016/J.ASEMS.2022.100030.

(31) Chen, C.; Yu, M.; Tong, J.; Xiong, L.; Li, Y.; Kong, X.; Liu, J.; Li, S. A Review of Fluorescence Based Corrosion Detection of Metals. *Corros. Commun.* **2022**, *6*, 1–15. https://doi.org/10.1016/J.CORCOM.2021.11.009.

(32) Chakri, S.; Patel, A. N.; Frateur, I.; Kanoufi, F.; Sutter, E. M. M.; Tran, T. T. M.; Tribollet, B.; Vivier, V. Imaging of a Thin Oxide Film Formation from the Combination of Surface Reflectivity and Electrochemical Methods. *Anal. Chem.* **2017**, *89* (10), 5303–5310. https://doi.org/10.1021/acs.analchem.6b04921.

(33) Godeffroy, L.; Aguilar, I.; Médard, J.; Larcher, D.; Tarascon, J.-M.; Kanoufi, F. Decoupling the Dynamics of Zinc Hydroxide Sulfate Precipitation/Dissolution in Aqueous Zn–MnO 2 Batteries by Operando Optical Microscopy: A Missing Piece of the Mechanistic Puzzle. *Adv. Energy Mater.* **2022**, *12* (n/a), 2200722. https://doi.org/10.1002/aenm.202200722.

(34) Young, G.; Kukura, P. Interferometric Scattering Microscopy. *Annu. Rev. Phys. Chem.* **2019**, *70* (1), 301–322. https://doi.org/10.1146/annurev-physchem-050317-021247.

(35) Taylor, R. W.; Sandoghdar, V. Interferometric Scattering Microscopy: Seeing Single Nanoparticles and Molecules via Rayleigh Scattering. *Nano Lett.* **2019**, *19* (8), 4827–4835. https://doi.org/10.1021/acs.nanolett.9b01822.

(36) Shan, X.; Díez-Pérez, I.; Wang, L.; Wiktor, P.; Gu, Y.; Zhang, L.; Wang, W.; Lu, J.; Wang, S.; Gong, Q.; Li, J.; Tao, N. Imaging the Electrocatalytic Activity of Single Nanoparticles. *Nat. Nanotechnol.* **2012**, *7* (10), 668–672. https://doi.org/10.1038/nnano.2012.134.

(37) Merryweather, A. J.; Schnedermann, C.; Jacquet, Q.; Grey, C. P.; Rao, A. Operando Optical Tracking of Single-Particle Ion Dynamics in Batteries. *Nat. 2021 5947864* **2021**, *594* (7864), 522–528. https://doi.org/10.1038/s41586-021-03584-2.

(38) Merryweather, A. J.; Jacquet, Q.; Emge, S. P.; Schnedermann, C.; Rao, A.; Grey, C. P. Operando Monitoring of Single-Particle Kinetic State-of-Charge Heterogeneities and Cracking in High-Rate Li-Ion Anodes. *Nat. Mater.* **2022**, *21* (11), 1306–1313. https://doi.org/10.1038/s41563-022-01324-z.

(39) Hao, R.; Peng, Z.; Zhang, B. Single-Molecule Fluorescence Microscopy for Probing the Electrochemical Interface. *ACS Omega* **2020**, *5* (1), 89–97. https://doi.org/10.1021/acsomega.9b03763.

(40) Le Guern, F.; Mussard, V.; Gaucher, A.; Rottman, M.; Prim, D. Fluorescein Derivatives as Fluorescent Probes for PH Monitoring along Recent Biological Applications. *Int. J. Mol. Sci.* **2020**, *21* (23), 1–23. https://doi.org/10.3390/IJMS21239217.

(41) Alodan, M. A.; Smyrl, W. H. Detection of Localized Corrosion of Aluminum Alloys Using Fluorescence Microscopy. *J. Electrochem. Soc.* **1998**, *145* (5), 1571–1577. https://doi.org/10.1149/1.1838520.

(42) Birbilis, N.; Buchheit, R. G. Electrochemical Characteristics of Intermetallic Phases in Aluminum Alloys. *J. Electrochem. Soc.* **2005**, *152* (4), B140. https://doi.org/10.1149/1.1869984.

(43) L., N.; Zhou, X.; Birbilis, N.; Hughes, A. E.; C. Mol, J. M.; J., S.; Zhou, X.; E., G. Durability and Corrosion of Aluminium and Its Alloys: Overview, Property Space, Techniques and Developments. *Alum. Alloy. - New Trends Fabr. Appl.* **2012**. https://doi.org/10.5772/53752.

(44) Örnek, C.; Liu, M.; Pan, J.; Jin, Y.; Leygraf, C. Volta Potential Evolution of Intermetallics in Aluminum Alloy Microstructure Under Thin Aqueous Adlayers: A Combined DFT and Experimental Study. *Top. Catal.* **2018**, *61* (9–11), 1169–1182. https://doi.org/10.1007/s11244-018-0939-9.

(45) Puigdomenech, I. Chemical Equilibrium Diagrams https://sites.google.com/site/chemdiagr/home (accessed Mar 2, 2015).

(46) Li, N.; Dong, C.; Man, C.; Yao, J. In Situ Electrochemical Atomic Force Microscopy and Auger Electro Spectroscopy Study on the Passive Film Structure of 2024-T3 Aluminum Alloy Combined with a Density Functional Theory Calculation. *Adv. Eng. Mater.* **2019**, *21* (12), 1900386. https://doi.org/10.1002/ADEM.201900386.

(47) Cornette, P.; Zanna, S.; Seyeux, A.; Costa, D.; Marcus, P. The Native Oxide Film on a Model Aluminium-Copper Alloy Studied by XPS and ToF-SIMS. *Corros. Sci.* **2020**, *174*, 108837. https://doi.org/10.1016/J.CORSCI.2020.108837.

(48) Olefjord, I.; Mathieu, H. J.; Marcus, P. Intercomparison of Surface Analysis of Thin Aluminium Oxide Films. *Surf. Interface Anal.* **1990**, *15* (11), 681–692. https://doi.org/10.1002/SIA.740151108.

(49) Yoo, J. D.; Ogle, K.; Volovitch, P. The Effect of Synthetic Zinc Corrosion Products on Corrosion of Electrogalvanized Steel. II. Zinc Reactivity and Galvanic Coupling Zinc/Steel in Presence of Zinc Corrosion Products. *Corros. Sci.* **2014**, *83*, 32–37. https://doi.org/10.1016/j.corsci.2013.12.024.

(50) Liu, L.; Xu, Y.; Zhu, Y.; Wang, X.; Huang, Y. The Roles of Fluid Hydrodynamics, Mass Transfer, Rust Layer and Macro-Cell Current on Flow Accelerated Corrosion of Carbon Steel in Oxygen Containing Electrolyte. *J. Electrochem. Soc.* **2020**, *167* (14), 141510. https://doi.org/10.1149/1945-7111/ABC6C8.

(51) Thomas, S.; Cole, I. S.; Sridhar, M.; Birbilis, N. Revisiting Zinc Passivation in Alkaline Solutions. *Electrochim. Acta* **2013**, *97*, 192–201. https://doi.org/10.1016/j.electacta.2013.03.008.

(52) Valavanis, D.; Ciocci, P.; Meloni, G. N.; Morris, P.; Lemineur, J.-F.; Mcpherson, I. J.; Fr´, F.; Fréd´, F.; Kanoufi, F.; Unwin, P. R. Hybrid Scanning Electrochemical Cell Microscopy-Interference Reflection Microscopy (SECCM-IRM): Tracking Phase Formation on Surfaces in Small Volumes. *Faraday Discuss.* **2022**, *233*, 122–148. https://doi.org/10.1039/D1FD00063B.

(53) Saha, P.; Hill, J. W.; Walmsley, J. D.; Hill, C. M. Probing Electrocatalysis at Individual Au Nanorods via Correlated Optical and Electrochemical Measurements. *Anal. Chem.* **2018**, *90* (21), 12832–12839. https://doi.org/10.1021/acs.analchem.8b03360.

(54) Wang, Y.; Shan, X.; Wang, S.; Tao, N.; Blanchard, P. Y.; Hu, K.; Mirkin, M. V. Imaging Local Electric Field Distribution by Plasmonic Impedance Microscopy. *Anal. Chem.* **2016**, *88* (3), 1547–1552. https://doi.org/10.1021/acs.analchem.5b04382.

(55) Tetteh, E. B.; Valavanis, D.; Daviddi, E.; Xu, X.; Santos, C. S.; Ventosa, E.; Martín-Yerga, D.; Schuhmann, W.; Unwin, P. R. Fast Li-ion Storage and Dynamics in TiO2

Nanoparticle Clusters Probed by Smart Scanning Electrochemical Cell Microscopy. *Angew. Chemie Int. Ed.* **2022**. https://doi.org/https://doi.org/10.1002/anie.202214493.

Supporting Information

Imaging and quantifying the chemical communication between single particles in metal alloy

Louis Godeffroy, Aleksei Makogon, Sarra Gam Derouich, Frédéric Kanoufi*, Viacheslav Shkirskiy*

Université Paris Cité, ITODYS, CNRS, 75013 Paris/France

frederic.kanoufi@univ-paris-diderot.fr, viacheslav.shkirskiy@cnrs.fr

Table of content

Description of supplementary videos:

Movie S1: Enlarged view (marked with square in Movie S2) of the surface film transformation on Al6061 during immersion in 10 mM H_2SO_4 with the movie snapshots at 17 s, 28 s, 37 s and 84 s, and related SEM image of identical location.

Movie S2: Wide-field view of surface films transformation on Al6061 during immersion in 10 mM H_2SO_4 and related SEM image of identical location. The area, around which the narrative in the manuscript is built, is highlighted with the square.

SI-1 Experimental part

Sample preparation

A foil of aluminum 6061-T6 alloy (Al6061), provided by Goodfellow, was cut into *ca.* 20 mm × 6 mm rectangle, which was mount in a carbon-based conductive mount (KonductoMet^{TM} 20-3375-016). The sample was polished successively with 320, 400, 600, 1200 grit SiC cooled with tap water. The final polishing step employed a polishing cloth (Presi^{TM}) with 30 nm alumina suspension (Presi^{TM}). The sample was then washed in acetone and deionized water, before being gently blown dry. Then, the sample was left under atmospheric conditions for *ca.* 1 week to spontaneously oxidize the Al interface in a humid O_2 containing environment and thus, to form a layer of surface oxides/hydroxides.[1–3] The Al surface was also manually marked in a grid with a scalpel to provide a visual reference for the identification of analyzed surface area. Just before the optical experiment, the surface was again washed with deionized water and gently blown dry.

In-situ fluorescence microscopy

A glass slice with deposited on it a 2 µL droplet of 10 mM H_2SO_4 saturated with fluorescein isothyocyanate FITC (Sigma Aldrich, HPLC purity) was placed on the top of the inverted microscope. The solubility of FTIC in water was found to be less than 0.1 mg/ml or 0.2 mM. The polished sample was placed on a 2 µL droplet and gently pressed against the glass slice, forming a thin layer of electrolyte (estimated thickness of *ca.* 25 µm) between transparent glass and metal interface. Firstly, we registered the images of reflected light, coming from the sample to find the region of interest and then we placed the cube filter to register fluorescence images. Fluorescence imaging was carried out on an inverted epifluorescence microscope (Olympus IC71) equipped with a ×40 0.6-NA air objective (Olympus LUMPlanFL N). The sample was illuminated with a white light source (Hg lamp) coupled through Olympus U-MSWB2 cube (with excitation filter within 450-480 nm and emission at 500 nm) to excite and reveal fluorescence emitted from the deprotonated FITC probe, occurring for pH higher than *ca.* 6 (Fig. S1).[1] A digital USB color camera (UI-3080CP Rev. 2, IDS with CMOS 2456×2054-pixel detector) collected the fluorescence emitted from the solution. FL images are recorded at a speed of 2 frames per second (fps) with 500 ms accumulation time. Data analysis was done on selected regions of interest using Python.

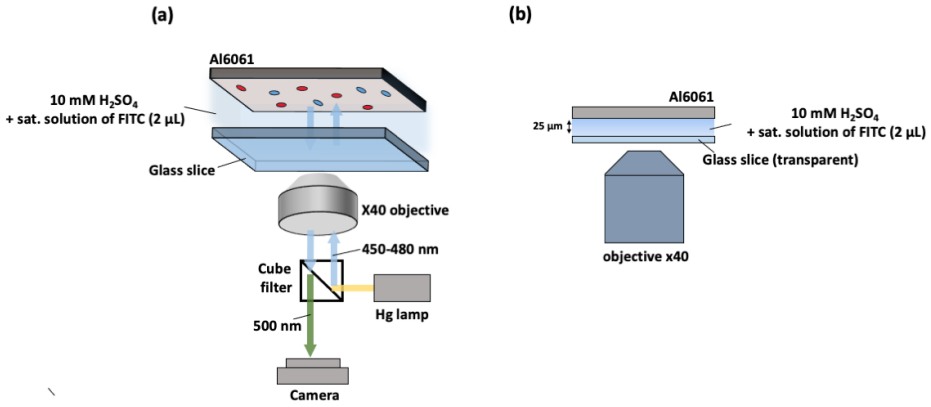

Fig. S1 *Schemes (not to scale) (a) of the entire setup for an operando fluorescence microscopy observation of the mirror polished Al6061 interface exposed to 10 mM H_2SO_4 + sat. FITC solution and (b) of the solution cell.*

In-situ reflective microscopy (RM)

The mirror polished Al6061 sample was fixed at the bottom of a cylindrical home-made cell with the circular exposed surface area of *ca.* 50 mm^2 and placed into RM setup with the light illumination/collection from the top. (Fig. S2) The details of an in-house developed RM setup can be found elsewhere.[4,5] Briefly, it consisted of an Olympus microscope, equipped with a water immersion objective (magnification ×60 1.00-NA (Olympus LUMPlanFL N)) with a focus distance of *ca.* 3 mm and a MV-D1024-160-CL-12 CCD camera (Photonfocus, 1024×1024 pixels, 14 bit). A halogen white lamp, filtered in the blue at 490 nm with an interference filter (spectral bandwidth of 20 nm), served as the light source. The low light intensity of ca. 2 mW cm^{-2} guaranteed a negligible heating of the studied interface to *ca.* 10^{-6} ^{o}C during the time of experiment. The substrate was illuminated from the top by the blue light beam via the microscope objective. The reflected light was collected by the same objective and sent to the CCD camera, which allows real time imaging of the light flux reflected by the analyzed surface. Before the experiment, planarity of the analyzed surface area (10^{-2} ^{o} precision) was achieved using an interference Mirau objective (magnification ×10 (CF Plan, Nikon)) via minimizing the interference fringes. Then, 20 mL of distilled water (MilliporeTM system, 18 MΩ×cm) was poured gently into the cell to expose the Al6061 interface to the liquid medium without causing much corrosion due to the low electrolyte conductivity. After focus adjustments in distilled water, image acquisition (at 0.5 Hz acquisition rate) was started and a concentrated solution of 1 mL H_2SO_4 (analytical grade, VWR) was gently added to the distilled water in the cell to provide 10 mM H_2SO_4 final concentration. Each acquired image consisted of a stack of 4 snapshots, each integrated over 50 ms, for a total duration of 200 ms. After ca. 3 min, the image acquisition was stopped, the substrate was removed and dried under Ar flow.

The image processing was performed in two steps. At the beginning, 4 particles were identified in each corner of the reflectivity map, then the reflectivities over these particles were fitted to a 2D-gaussian distribution and the maxima of this fit were extracted for each frame. The positions of the maxima for each particle did not vary more than 1 pixel that ensured insignificant thermal drift during image acquisition. Later, we located identical particles on SEM and EDX images (*vide infra*) using similar procedure of fitting to a 2D-gaussian distribution to further perform the alignment of *in-situ* RM and *ex-situ* SEM/EDX images with a pixel precision. All reflectivity maps were normalized by the intensities from the first reflectivity image and converted to the change of the thickness of surface films according to the Fresnel model described below. The image analysis was performed using Python scripts. Examples of image analysis, as well as the original data, are available in the Zenodo repository (https://doi.org/10.5281/zenodo.7963186) under a Creative Commons Attribution 4.0 International license.

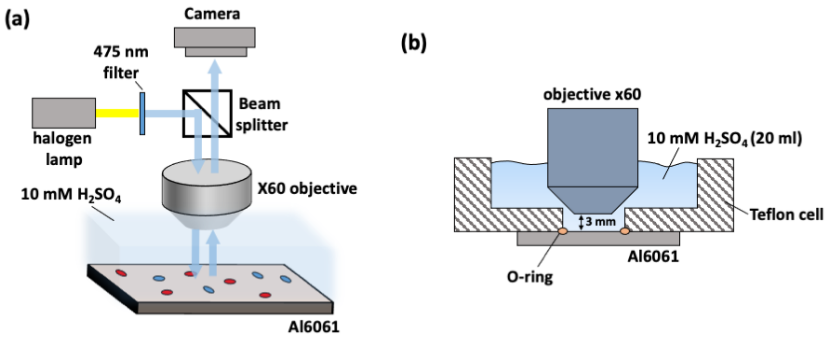

Fig. S2 *Schemes (not to scale) (a) of the entire setup for an operando reflective microscopy observation exposed to 10 mM H_2SO_4 and (b) of the solution cell.*

Description of the Fresnel model for the conversion of reflectivity changes to the changes of surface film thickness.[4,6]

In the case of a normal incidence, the light reflectivity (*R*) of an electromagnetic wave propagating in a medium A (characterized by its real index n_A) reflecting on a plane substrate S (characterized by its complex refractive index n_S), is the square of the modulus of the reflection coefficient and is given by eq. 1:

$$R_{AS} = |r_{AS}|^2 = \left|\frac{n_A - n_S}{n_A + n_S}\right|^2 \quad (1)$$

When an intermediate thin film of thickness δ (with refractive index n_F) is formed between the substrate and the medium (such as an aluminum oxide/hydroxide film which is located between the Al6061 interface and the electrolytic solution), the expression of the light reflectivity can be expressed as

$$R_{AFS} = \left|\frac{r_{AF} + r_{FS} e^{2i^{2\pi}/\lambda n_F \delta}}{1 + r_{AF} r_{FS} e^{2i^{2\pi}/\lambda n_F \delta}}\right|^2 \quad (2)$$

where λ is the wavelength of the incident light, $i = \sqrt{-1}$, and r_{AF} and r_{FS} are the reflection coefficients at the medium A/surface film and surface film/substrate interfaces, respectively. The intensity of the reflected light as a function of time ($I_r(t)$) normalized by the light intensity at *t=0* ($I_r(0)$) is then linked to the relative variation of the reflectivity as

$$\frac{I_r(t)}{I_r(0)} = 1 + \frac{\Delta R_{AFS}}{R_{AFS}(t)} \quad (3)$$

where $\Delta R_{AFS} = R_{AFS}(t) - R_{AFS}(t = 0)$.

Fig. S3a illustrates the variations in relative reflectivity calculated with eq. 2 for $Al/Al(OH)_3/H_2O$ interface. A nearly linear correlation is observed between the change in the thickness of the surface film and the relative reflectivity with the calibration factor found as 0.1 % light intensity change corresponds to a 1 nm change in δ. This sensitivity factor was used throughout this manuscript.

Note that the assumption is made that the layer formed at the Al surface is pure $Al(OH)_3$, reported as the most thermodynamically stable phase.[9] Using this assumption, the *ex-situ* ellipsometry measurements (SE 400adv ellipsometer (SENTECH)) provided a value of 10 nm surface film thickness of a naturally oxidized Al interface that is in in order of magnitude with the reported value of 3-5 nm, [2] provided from X-ray photoelectron spectroscopy (XPS). In addition, calculations of sensitivity of the calibration factor as a function of refractive index variations of surface films (Fig. S3b) shows that within the reported values of n_F (1.56-1.77 [7,8] for Al species such as Al_2O_3, AlO(OH) and $Al(OH)_3$ [1,3] and 1.46 [7] for SiO_2 sandwiched between Al and surface films in some analysed areas) the calibration factor should not vary more than 0.5 – 2 times. Altogether, this provides confidence in the optical model and defines limits in the estimation of absolute values of surface film thickness.

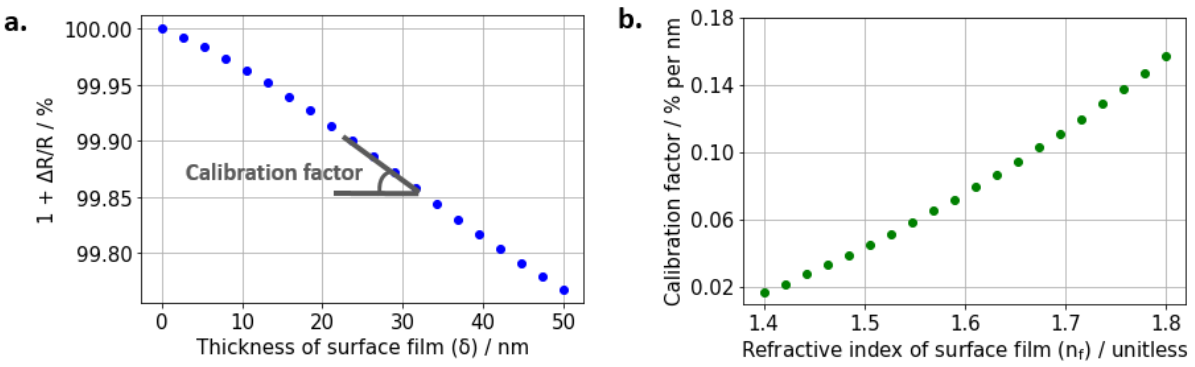

Fig. S3 *(a) Calculated change in reflectivity as a function of the surface film thickness using eq. 2 for Al/Al(OH)₃/H₂O interface at λ = 490 nm,* n_S^{Al} *= 0.46+4.69i,*[7] $n_F^{Al(OH)_3}$ *= 1.67* [8] *and* $n_A^{H_2O}$*=1.33.*[7,8] *(b) shows the sensitivity (ratio between reflectivity change in % per nm of surface film) as a function of the refractive index of surface film* n_F*.*

Ex-situ scanning electron microscopy (SEM)/energy-dispersive X-ray spectroscopy (EDX) surface analysis of identical locations

Identical locations of optical images were retrieved in secondary electron images during SEM analysis with the aid of grid marked on the Al6061 surface. SEM and EDX analyses were performed on a Gemini SEM 360 from Zeiss, with an acceleration voltage of 10 kV and 5 kV correspondingly, and 60 µm aperture window. Spectra and elemental mappings were processed using the AZtec software. The alignment to a pixel precision of optical and SEM/EDX images were performed with the automated feature-based algorithms implemented in OpenCV library, described in detail in ref [10].

Ex-situ atomic force microscopy (AFM)

Atomic force microscopy (AFM) experiments were performed using the NT-MDT AFM Instruments, installed on a dynamic anti-vibration device. Imaging of Al6061 surface was performed in air using standard tapping AFM mode, with Al-coated silicon probes from Nanosensors (cantilevers 40 ± 10 N/m spring constant and 290 ± 10 kHz resonance frequency). The pyramid-shaped tips had a radius of curvature of less than 10 nm. Topographic images were recorded at scan rates of 1 or 0.5 Hz. Image processing (flatten, plane fit, edge, and profiles, etc.) was performed with the WSXM processing software. At least three different areas of each sample were scanned, and typical images were presented. Values of nanoparticles height and size were determined.

X-ray diffraction (XRD) analysis

The XRD measurements were performed on a Panalytical X'pert pro diffractometer equipped with a Co anode ($\lambda_{K\alpha}$ = 1.79031 Å) and a multichannel X'celerator detector. The diffraction peaks were attributed using the HighScore Plus software.

SI-2 Finite Element Method (FEM) simulations of particle crosstalk

The FEM model was built in a 3D geometry with COMSOL Multiphysics 5.5 software (1) to simulate the steady-state pH distribution and (2) to simulate the transients of $Al(OH)_3$ dissolution/precipitation in the case of galvanic corrosion of Fe- and Si-rich particles dispersed in Al matrix of Al6061 alloy. The geometry of simulated area (Fig. S4) was chosen to mimic the particle positioning observed in in-situ RM experiment: Si-rich particle is represented by a 2 µm in diameter disk (2D) while Fe-rich particles are 3 small disks (2D) of 1 µm in diameter located on the same side relative to Si-rich area, all positioned at the bottom of the simulation box in the shape of hemisphere. Note that we do not aim to reproduce the exact conditions (particle sizes, shapes, and positions) since in any case, other parameters (local potential and current distributions) were not accessible experimentally. Opposed to that, we use simulations to only illustrate the underlying physical principles that can explain the observed distribution of the precipitation kinetics of surface films over a Si-rich particle.

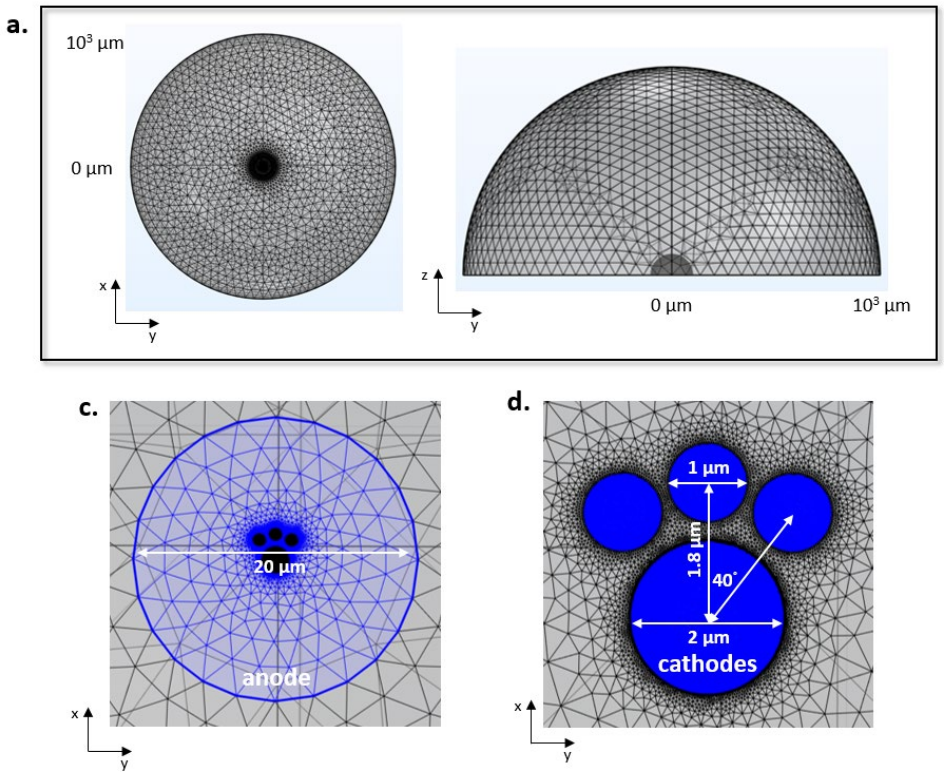

Fig. S4 *Geometry (up to scale) of the simulated box in FEM model. (a) show the whole view in xy and zy planes while (c) is the zoom of the whole electroactive area located at the bottom of simulated hemisphere (the anode area is highlighted with blue) and (d) is the zoom around 2D disks, where the cathode areas are highlighted in blue. Triangles represent free tetrahedral meshing employed in the model.*

In both types of simulations, the 2D disks were set to generate OH^-, representing local cathodes, while the rest of the area within 10 µm radius was set to produce Al^{3+}, representing anode of the galvanically coupled corrosion around Fe- and Si-rich particles. Diffusion coefficients of all species were set to 10^{-9} m^2/s. The initial concentration of OH^- in the bulk as well as the constant boundary OH^- concentration (top surface of the hemisphere) were set to 10^{-9} mol/m^3. The electrolyte conductivity was set to 0.5 S/m. Both values should closely mimic 10 mM H_2SO_4 aqueous solution.

In the first type of simulations (steady-state), two modules were used: "secondary current distribution" to account for the formation of galvanic couplings between cathodic and anodic zones and "transport of diluted species" to account for the diffusive transport of electrochemically generated species. The considered electrochemical reactions are galvanically coupled Al dissolution and oxygen reduction reaction (ORR):

$$\text{Anode:} \qquad Al \rightarrow Al^{3+} + 3e^- \tag{4}$$

$$\text{Cathode:} \qquad O_2 + 2H_2O + 4e^- \rightarrow 4OH^- \tag{5a}$$

$$2H_2O + 2e^- \rightarrow H_2 + 2OH^- \tag{5b}$$

The kinetics of two types of reactions were described with anodic and cathodic Tafel equations:

$$j_{loc} = j_0 \times 10^{\eta/a} \tag{6}$$

where j_{loc} is the local current density, i_0 is the exchange current density, a is the Tafel slope and η is the overpotential defined as the difference between equilibrium and imposed potentials ($\eta = E_{eq} - E$). The anodic currents were considered to be positive, and the cathodic ones were negative by convention. The electrochemical constants were taken within the range of values reported in the literature for Al alloy and Fe- and Si-rich phases.[15,16,22–24] The used values are reported in Table S1.

Table S1. *Input electrochemical constants for steady-state FEM simulations*

Type of boundary	j_0 / (A/cm^2)	E_{eq} / (V)	a / (mV/decade)
2 µm disk (cathode)	5.7×10^{-5}	-0.6	-300
1 µm disks (cathode)	5.1×10^{-4}	-0.55	-370
the rest (anode)	10^{-4}	-0.7	50

The results of steady-state simulations were used to estimate the pH distribution on disk areas, presented in the main text (Fig. 3, right). Also, we noticed that the formation of galvanic couple computed in "secondary current distribution module" leads to a nearly homogeneous flow on electrochemically active boundaries: 1.74×10^{-5} mol/(m^{2}s) on the 2 µm and 1.74×10^{-4} mol/(m^{2}s) of OH^- on the 1 µm disks, and 1.59×10^{-6} mol/(m^{2}s) of Al^{3+} on the rest of the surface (Fig. S5). It was due to sufficient electrolyte conductivity to minimize for the Ohmic drop between the anode and the cathodes areas.

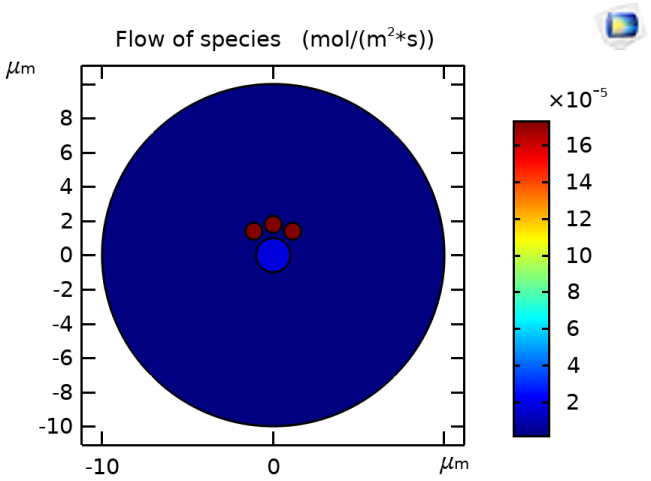

Fig. S5 *Flow of species on the electrochemically active regions.*

Therefore, in the next set of simulations (transient), we simplified the model using only "transport of diluted species" module and the aforementioned values of fluxes as boundary conditions to reduce the time of the calculations and improve on convergence. We also introduced the precipitation and dissolution of $Al(OH)_3$ species as the boundary conditions on the anodic and cathodic sites (Fig. S4) according to chemical reactions:

$$Al^{3+} + 3OH^- \leftrightarrow Al(OH)_3 \quad (7)$$

$$Al(OH)_3 + OH^- \leftrightarrow Al(OH)_4^- \quad (8)$$

To implement this in Comsol, general form boundary partial differential equation (PDE) was added in the form of first order PDE: $\partial C\{Al(OH)_3\}/\partial t = r$, where $C\{Al(OH)_3\}$ is the surface concentration of $Al(OH)_3$ and r is the rate of its formation. r was defined as $r = r_7 + r_8$ where

$$r_7 = k'\left(C_{Al}C_{OH}^3 - K'\right) \quad (9)$$

$$r_8 = k''\left(C_{AlOH_4}/K'' - C_{OH}\right) \quad (10)$$

C_{Al}, C_{OH} and C_{AlOH_4} are the solution activities of Al^{3+}, OH^- and $Al(OH)_4^-$ defined as their concentrations normalized by 1 M; K' is the solubility constant of $Al(OH)_3$, K'' is the complexation constant of $Al(OH)_4^-$, k' and k'' are the kinetic constants of reactions (3) and (4) correspondingly. K' = 10^{-33} and K'' = 0.257 were retrieved from the database of chemical equilibrium software [9] while $k' = 4.5\times10^{27}$ mol/(m^{2}s) and $k'' = 1.0\times10^{10}$ mol/(m^{2}s) were chosen empirically to provide the best fit of experimental data on the evolution of surface films (Fig. 2b in the manuscript). The initial concentration of $C\{Al(OH)_3\}$ was set to 3.1×10^{-4} mol/m^2 that corresponds to the experimentally measured (*vide supra*) 10 nm surface oxide/hydroxide layer, taking into account the density of $Al(OH)_3$ as 2.42 g/cm^3. Finally, the input fluxes of OH^- and Al^{3+} were multiplied by an empirical parameter *p* that equaled to 0 between 0 s - 20 s then 0.23 between 20 s - 53 s and 1.0 between 53 s - 120 s. In this way, we provided the transition between different regimes of surface film evolution observed experimentally in Fig. 2b. The exact physical reason of parameter *p* is not known. Some literature suggests that the thickness, composition, and structure of dynamically evolving surface films can have an impact on kinetics of cathodic reactions.[25–27] All of it is discussed in detail in the manuscript, showing the results of the time-dependent simulations in Fig. 3b.

SI-3 Roughness of polished Al6061 sample

AFM image in Fig. S6 shows that roughness of mirror polished Al6061 is within 40 nm, particles and Al matrix considered altogether. This value is small enough (way below the diffraction limit) to consider the surface to be flat in optical models described in SI-1.

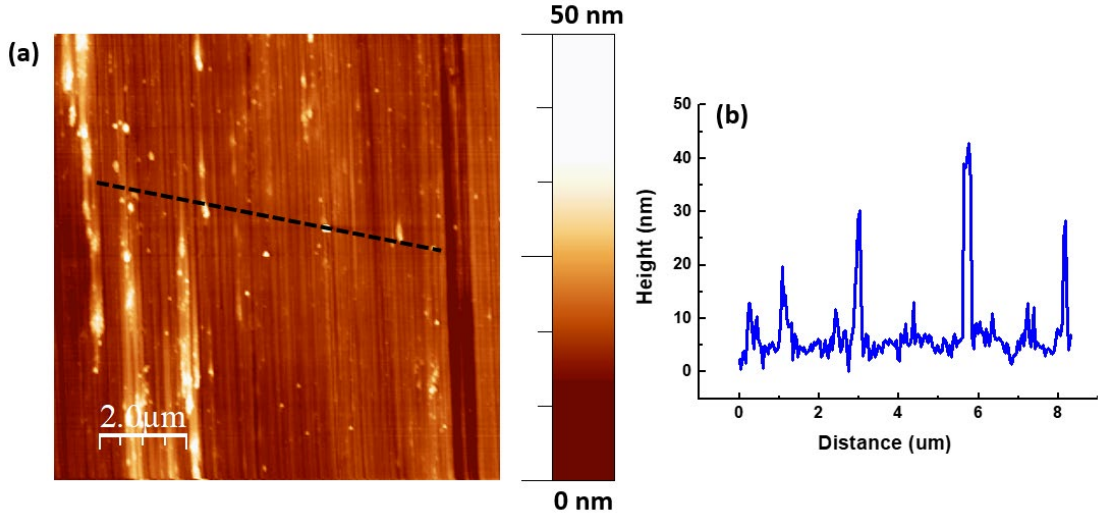

Fig. S6 *(a) Typical AFM image of mirror polished Al6061 samples and (b) is the 2D section along the back dash line in (a)*

SI-4 Comparison of surface states before and after immersion tests

Before the optical experiments, we tested the impact of 5 min exposure to 10 mM H_2SO_4 aqueous solution on the surface state of Al6061 interface. The SEM/EDX observations (Figs. S7-S11) reveal little to no difference in surface topography and chemical composition. This was supposedly due to the short time of exposure and low concentration of corrosive electrolyte that, according to the literature,[11–14] are very mild corrosive conditions.

Note that even though Mg signal was detected from the EDX map in Fig. S11, Mg species are not located on the interface (and do not contribute to the reactivity during the immersion tests). Cross correlation of identical locations in Fig. S12 shows no particles in the optical images and only fade contrast in SEM and Si EDX maps on spots where Mg signal is detected. Most likely Mg_2Si particles (supported with XRD in Fig. S13) are located in the bulk of Al6061 in a close proximity to the interface. For the reference, we used 10 kV and 5 kV acceleration voltage for SEM and EDX analysis correspondingly, that should give 0.1-1 µm penetration depth into the material bulk. The absence of Mg containing particles on the interface can be explained by selective dissolution of Mg from the Mg_2Si particles due to the metal interface polishing operated in the presence of water, as reported in ref [2].

Therefore, the as-prepared Al6061 interface is composed of Si, O-rich particles, and Fe-rich particles, which are identified as SiO_2 and Al_3Fe phases from XRD analysis in SI-5.

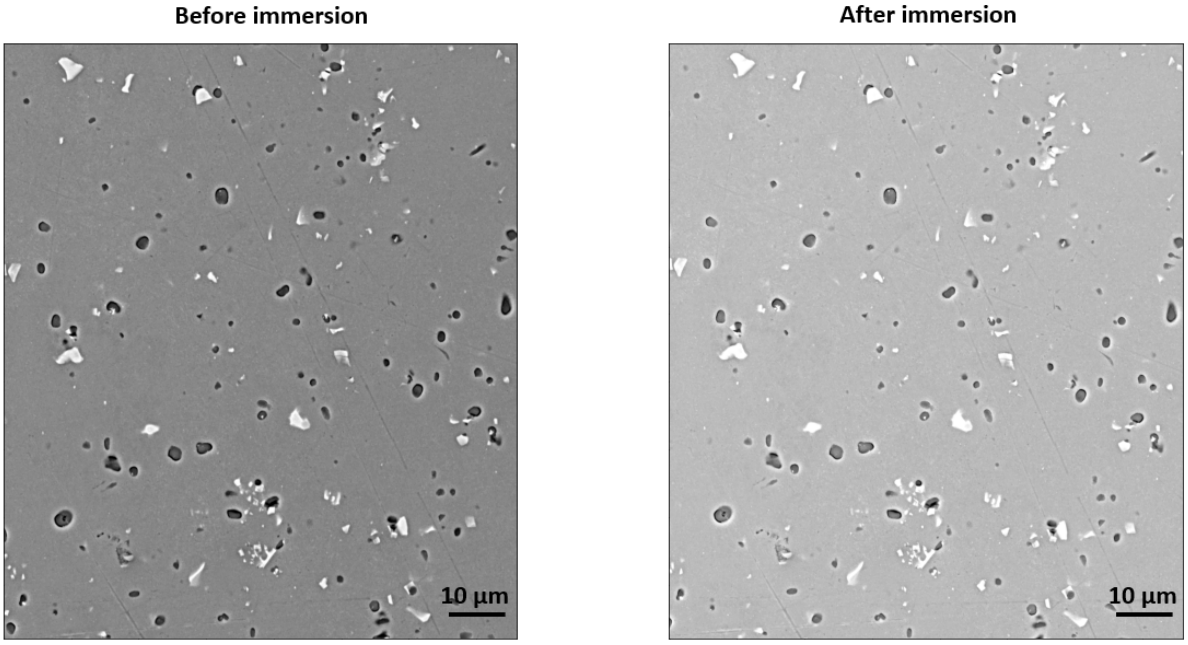

Fig. S7 *Representative SEM images of Al6061 surface before and after 5 min immersion in 10 mM H_2SO_4 aqueous solution. Slightly different contrast between images is due to contrast differences set in SEM image acquisition software and is not related to the differences in the surface states. Below we provide EDX maps of Si, O, Fe and Mg distribution.*

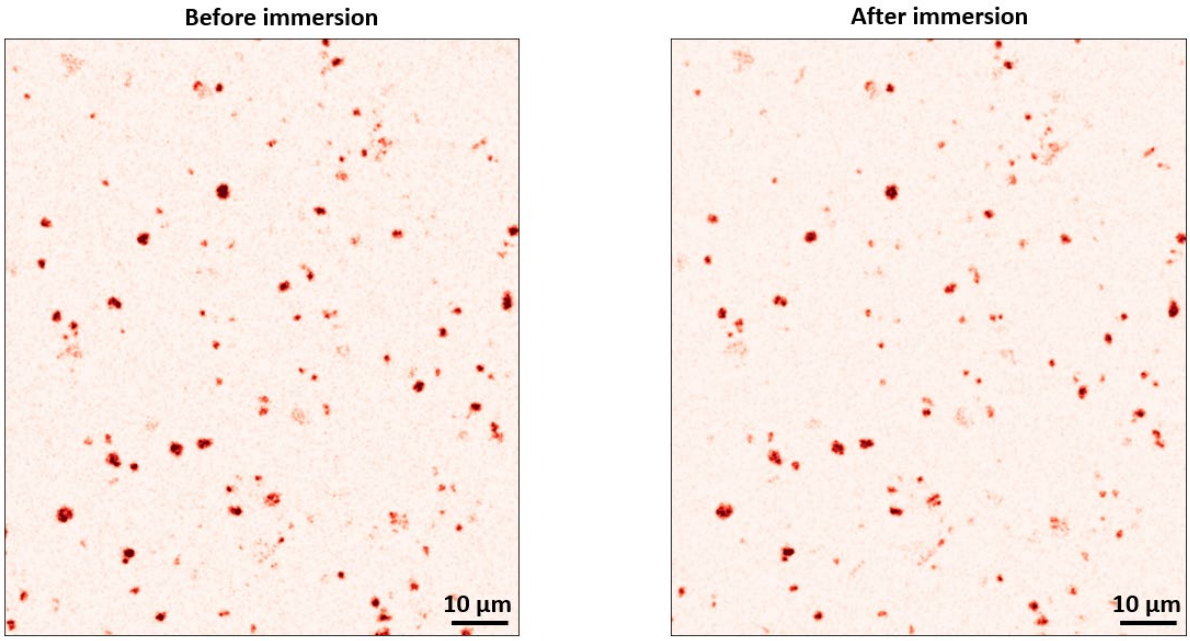

Fig. S8 *Si distribution from EDX mapping*

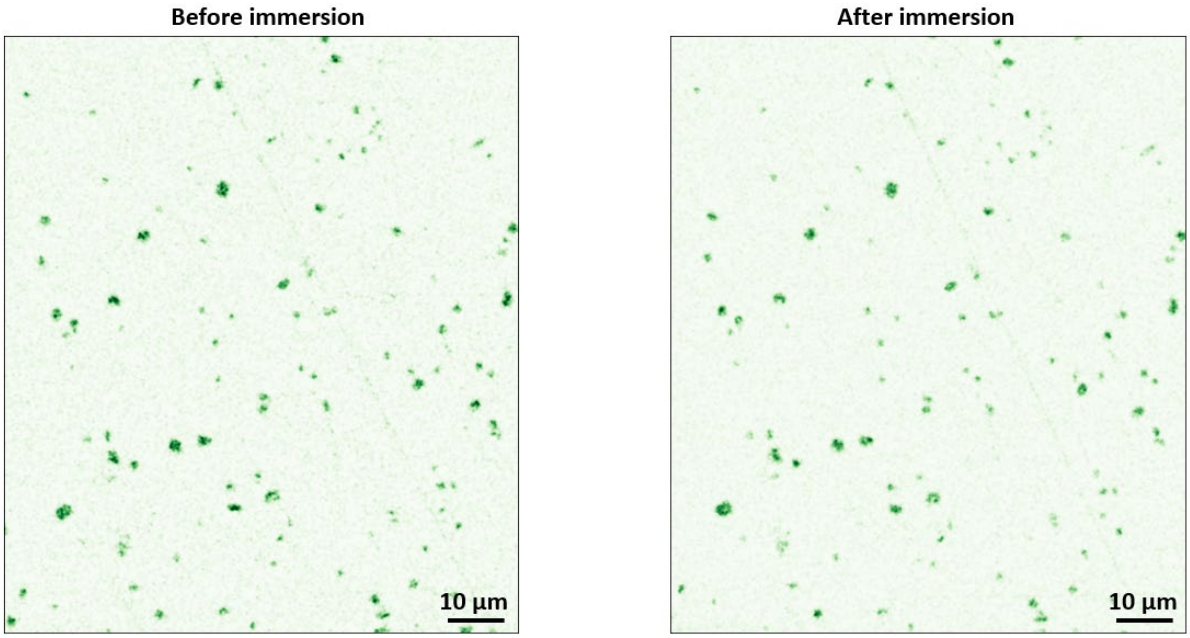

Fig. S9 *O distribution from EDX mapping*

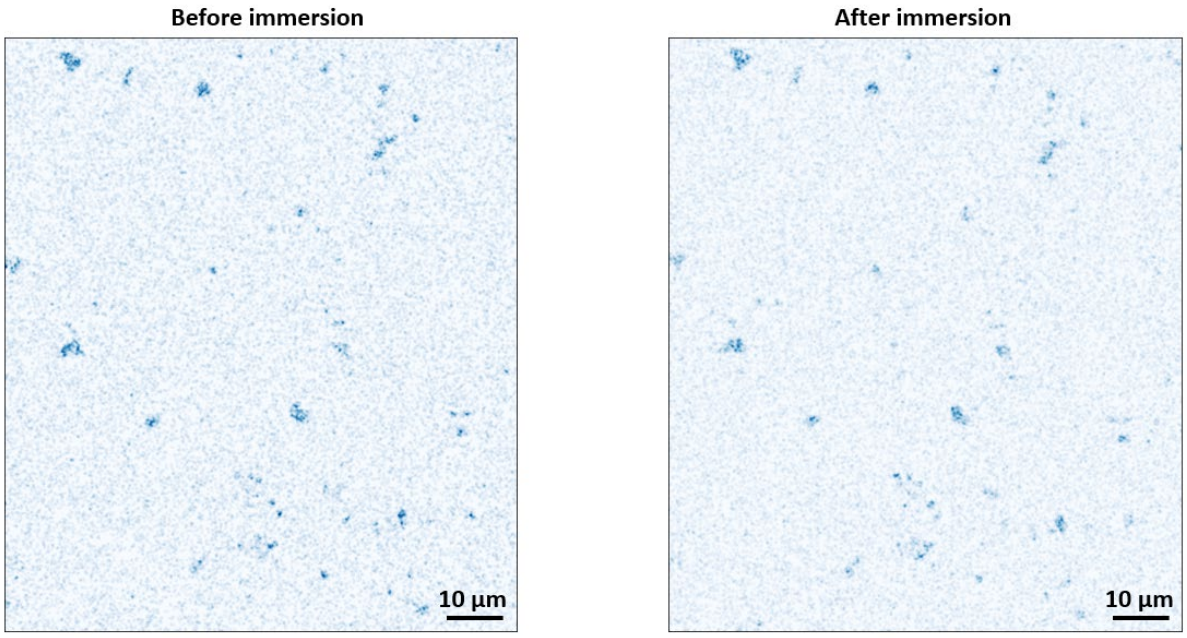

Fig. S10 *Fe distribution from EDX mapping*

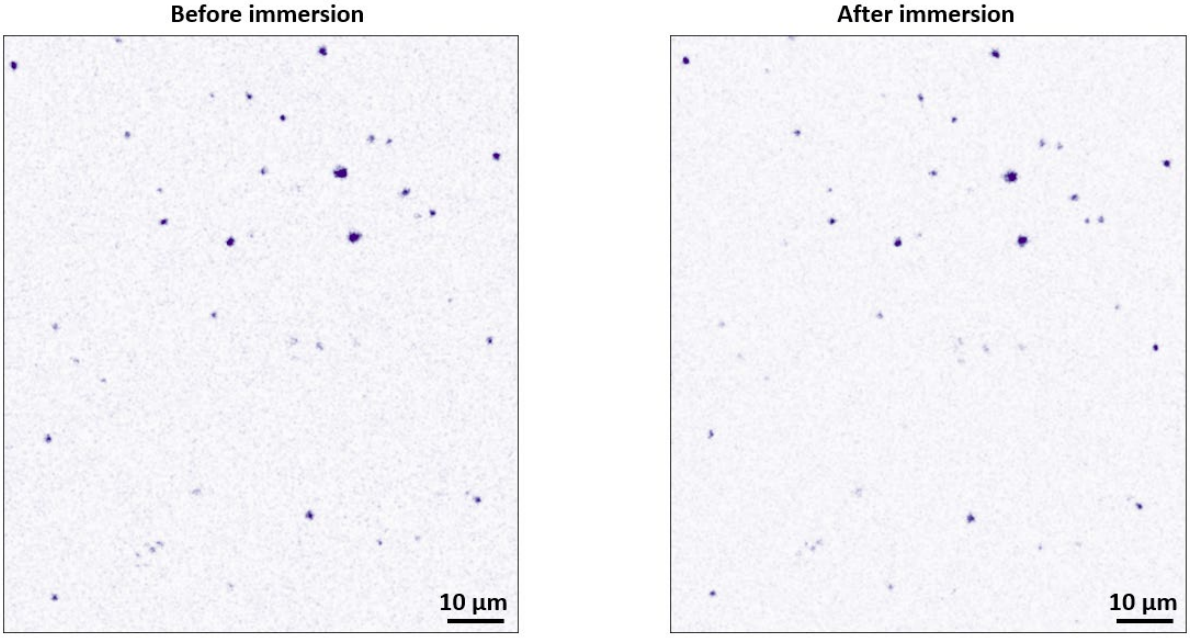

Fig. S11 *Mg distribution from EDX mapping*

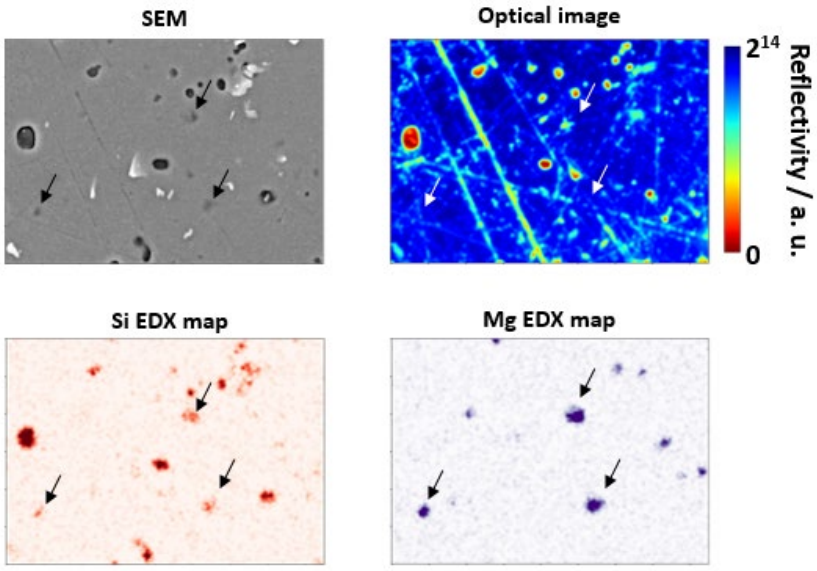

Fig. S12 *Zoom of the maps in Figs. S7-S11 shows SEM, Si, and Mg EDX maps complemented with an optical image. Identical locations, corresponding to the most intense Mg spots on the EDX map, are highlighted with arrows in all four images. A comparison of all the images suggests that the Mg signal comes from beneath the surface of the Al substrate.*

SI-5 Bulk material structure

The Al6061 sample was cut and embedded into the conductive resin matrix of cylindrical shape prior to any experiments (Fig. S13a), including XRD. This was to mount sample into a fully automated polishing equipment and thus, simplify polishing procedure crucial for operando RM experiments. Since the analysis volume of XRD is large, the diffractogram of Al6061 mounted sample contains the contribution from the resin that we ruled out by recording a separate diffractogram of pure resin (orange curves in Fig. S13). Analysis shows that crystalline graphite and SiO_2 make up for the signal from the resin, while the Al6061 is composed of Al crystalline, Mg_2Si, Al_3Fe, SiO_2 and Al_2O_3 (Fig. S13b). The particles of Mg_2Si and Al_3Fe are the main constituents of Al6061 bulk reported in the literature.[14–17] The SiO_2 and Al_2O_3 phases are located on the interface, that was partly oxidized during the polishing procedure (see SI-1 and the main text for details).

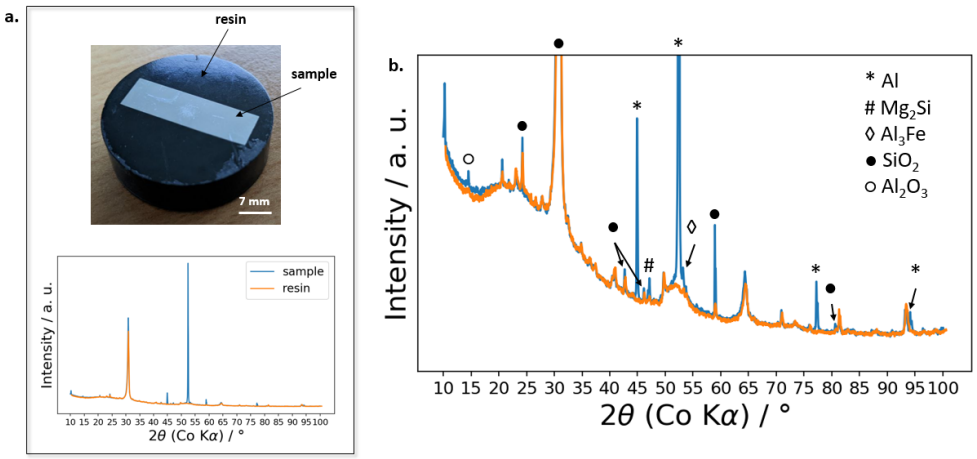

Fig. S13 *(a) Macroscopic picture of Al6061 sample placed into the resin (top) and the diffractograms of individual resin and sample embedded into resin (bottom). (b) Zoomed diffractogram with peak attribution: Al (ref ICSD 98-004-3492), Mg_2Si (ref ICSD 98-016-7510), Al_3Fe (ref.* [18]*), SiO_2 (ref ICSD 98-015-6198) and Al_2O_3 (ref ICSD 98-017-3014). Ensemble of small peak, related to resin, are not marked but attributed to graphite (ref ICSD 98-007-6767).*

SI-6 2D profile of reflectivity image over Fe-rich particle

The 2D profile of reflected light along the location of Fe-rich particle in Fig. S14c shows the decrease in intensity of the reflected light. It shows clearly that RM is sensitive enough to detect Fe-rich phases even though it might be hard to distinguish them looking at reflectivity images (Fig. S14a) due to high contrast between black and white regions. The main reason is that the Si-rich particles (dark regions) are strongly contrasted and with the whole sensitivity scale the Fe-rich particles may be invisible. Reflectivity (as ellipsometry) is a highly sensitive technique to local refractive index variations. The higher the image pixel depth (in bit) the higher the reflectivity sensitivity. For the dynamic analysis we used a 12 bit pixel (4096 a.u.) which allows a measurement with < 1% accuracy, especially when accumulating (stacking) successive images. In the Fig. 1 of the main manuscript, we use a less sensitive camera (8bit: 256 a.u.) as we would like to show the fluorescence/reflectivity coupled measurement.

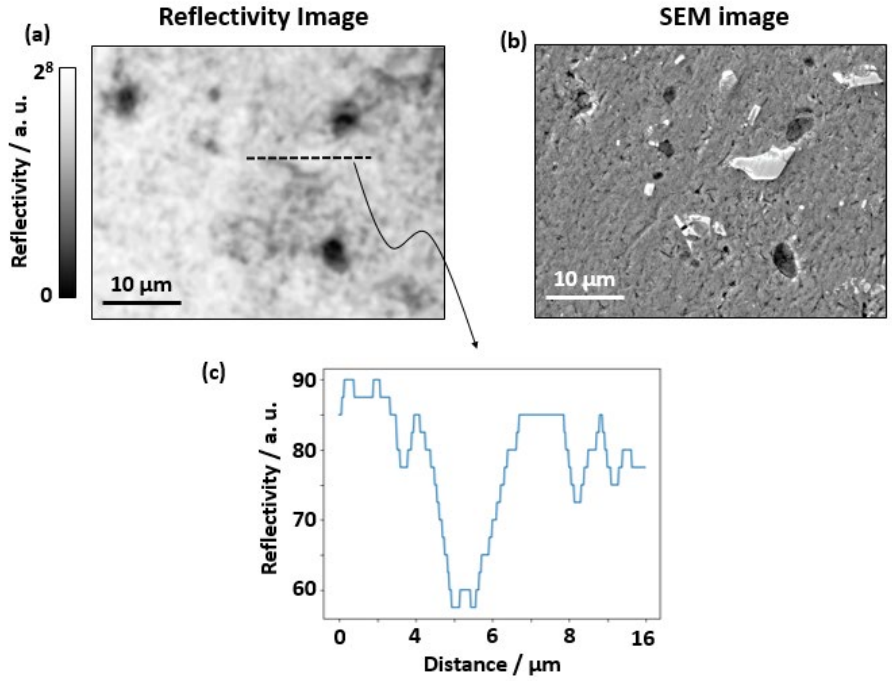

Fig. S14 *(a) Reflectivity and (b) SEM image of identical locations taken from Fig. 1b from the main manuscript. (c) presents the 2D profile of intensity of reflected light along the dash line in figure (a).*

SI-7 Wide-field view of analyzed interface

The total size of surface, analyzed in operando RM, is 110×170 μm^2. It is presented in Fig. S7-1 and Movie S1. Regions, where the crosstalk was suspected, consist of *ca.* 20 % of the analyzed interface. The total number of analyzed Fe-particles (with light contrast) and Si-rich particles (with dark contrast) is 710 and 479 correspondingly. The majority of particles are < 1 μm^2 in diameter.

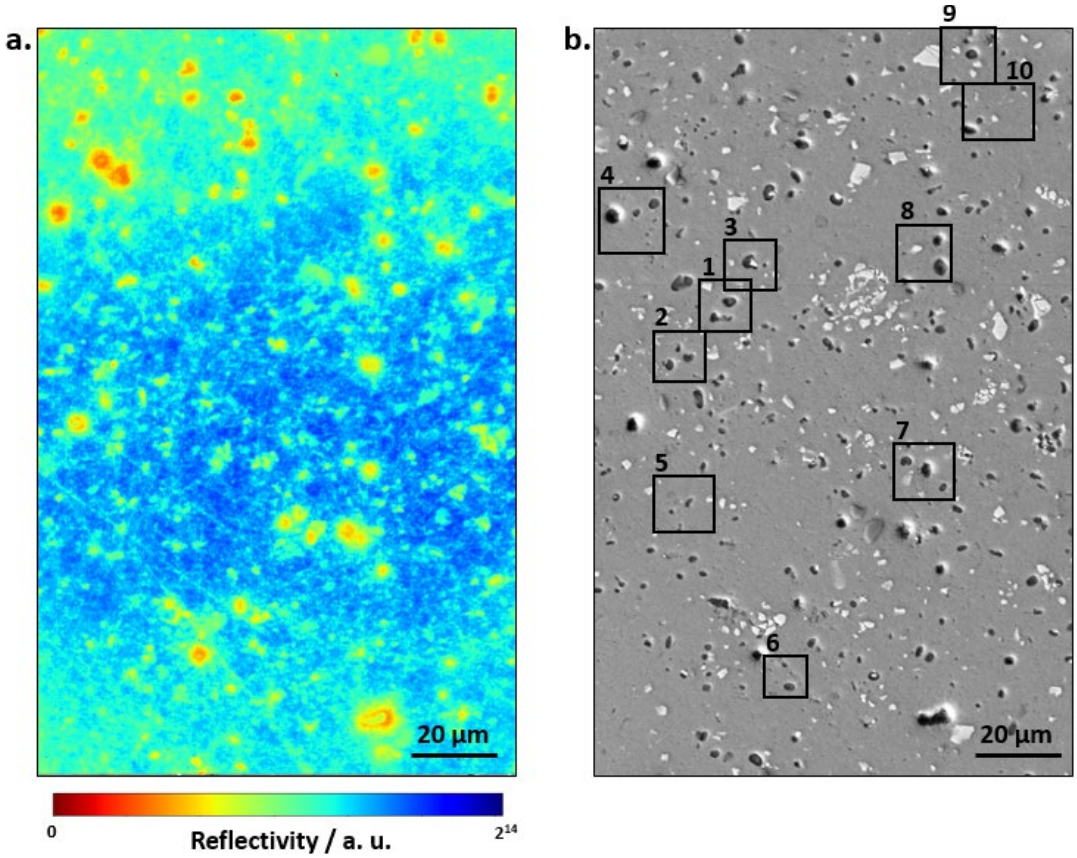

Fig. S15 *(a) Wide-field optical and (b) SEM images of analyzed Al6061 interface. Regions, where the crosstalk was suspected, are highlighted with rectangles.*

SI-8 Summary of the crosstalk appearances in the wife-field image

Table S2 *List of areas with the crosstalk appearances highlighted in Fig. S15 containing short description of the chemical communication manifests itself, cropped SEM image and 4 images of relative surface films thicknesses at different times are given.*

1. This example of the chemical communication is described in detail in the manuscript and provided in Movie S2. The chemical communication is visible from the appearance of dissolution (blue) and precipitation (red) regions on the single Si-rich particle (dark contrast in SEM image), presumably defined by the impact of neighboring Fe-rich particles (bright contrast in SEM image).
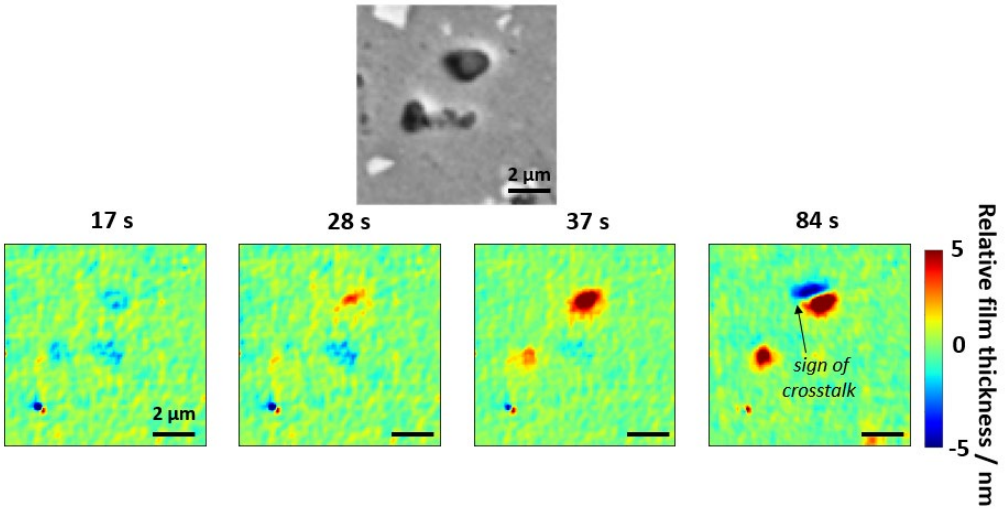
2. Similar to the 1st case.
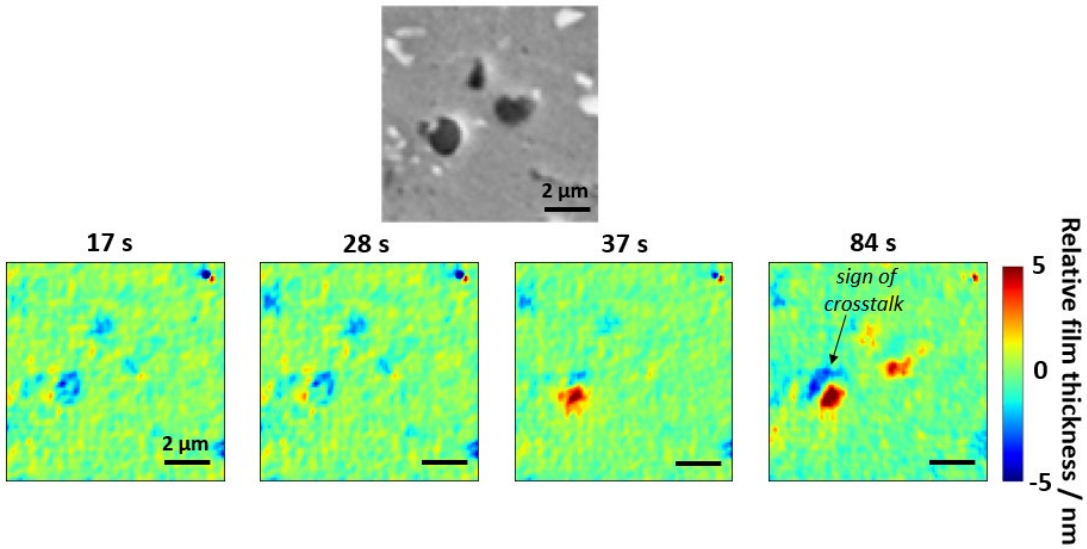
3. Similar to the 1st case.

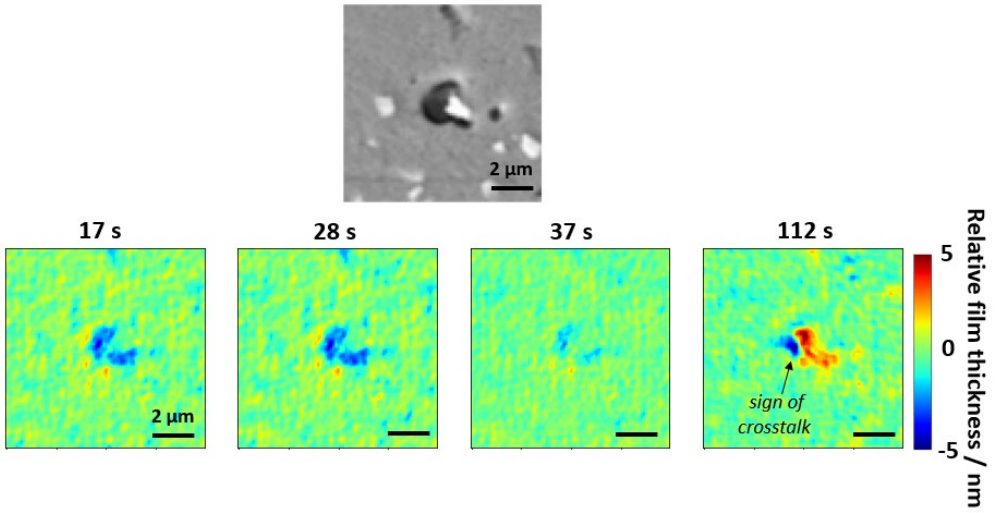

4. In this example, the neighboring Si-rich particles seems to have an impact on the evolution of surface layer on the neighboring Si-rich particle.

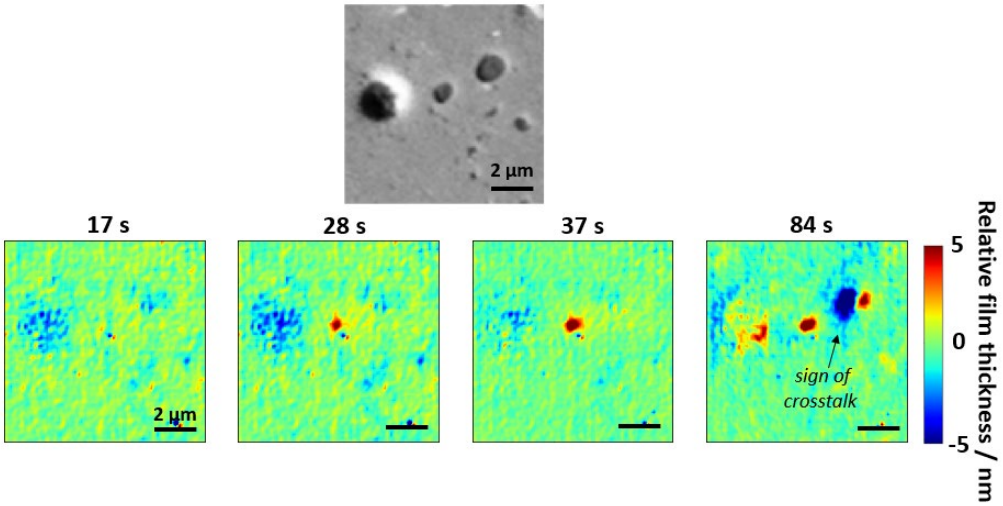

5. The separation of dissolution/precipitation regions on Si-rich particle becomes apparent early on in this area that can be related to the chemical communication between neighboring Si-rich particles.

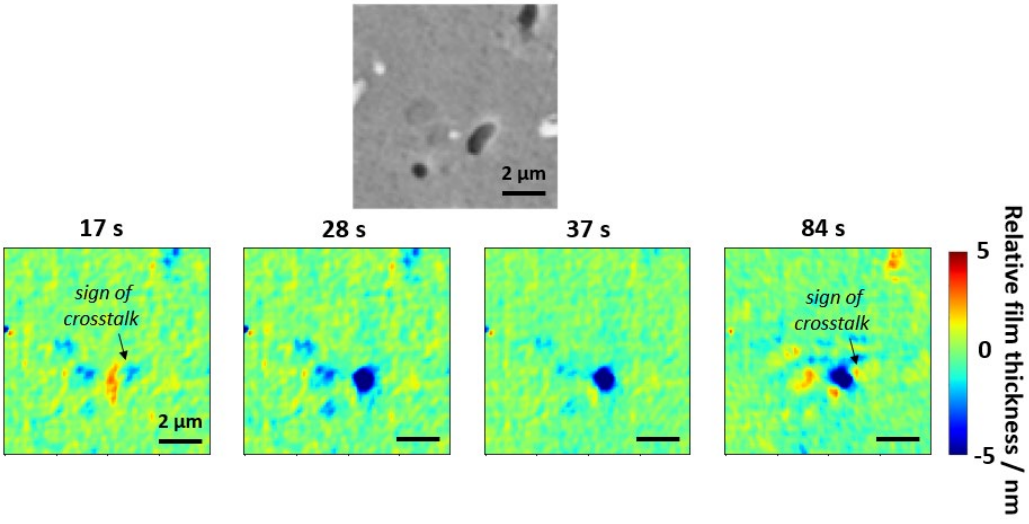

6. The chemical communication appears after 28 s of immersion and can be due to the presence

of sub micrometer Si-rich particles.

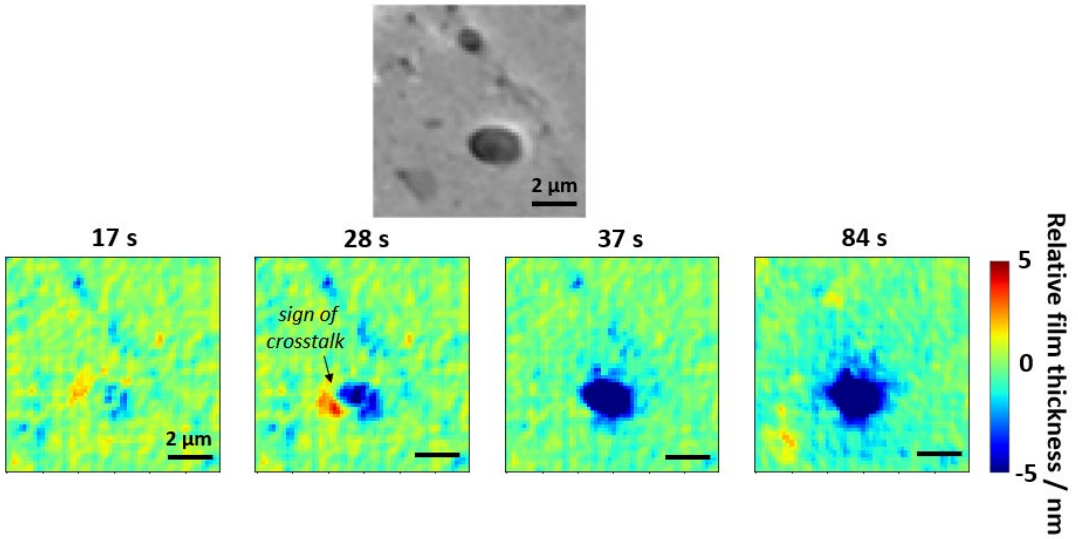

7. In this example, the separation of dissolution/precipitation is apparent on two neighboring particles that can be an indication of mutual impact on each other's activities.

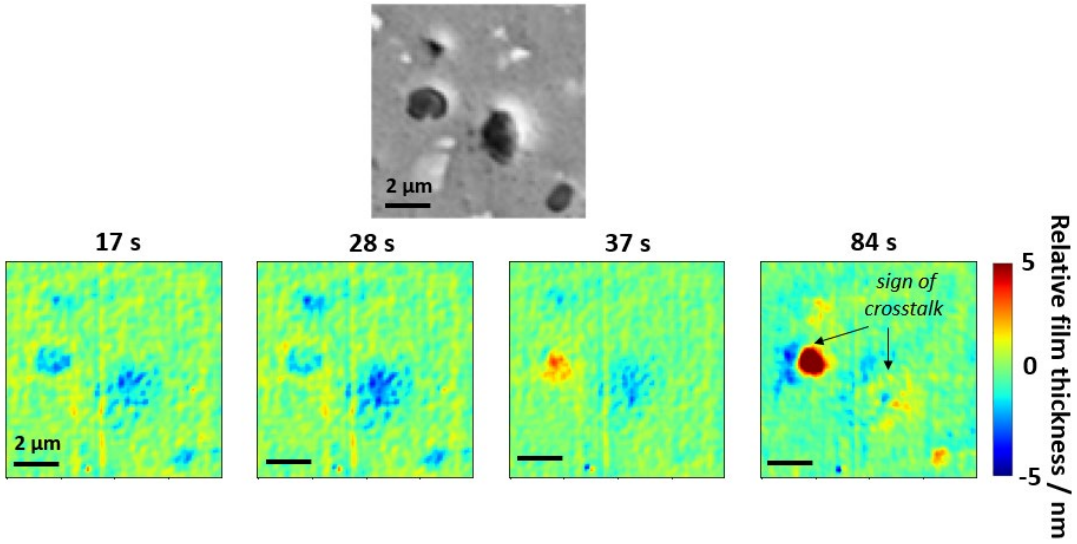

8. Similar to the 4th case.

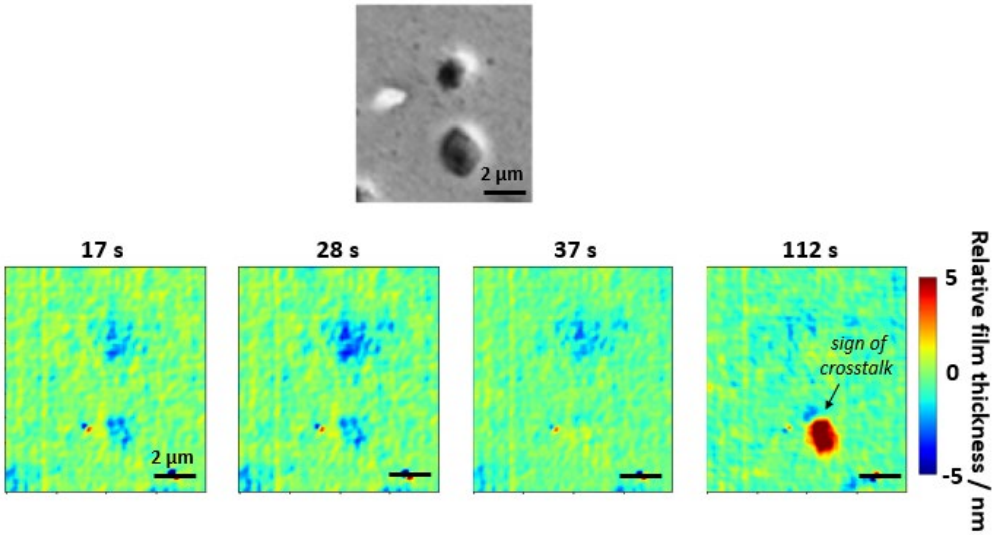

9. Similar to the 1st case.

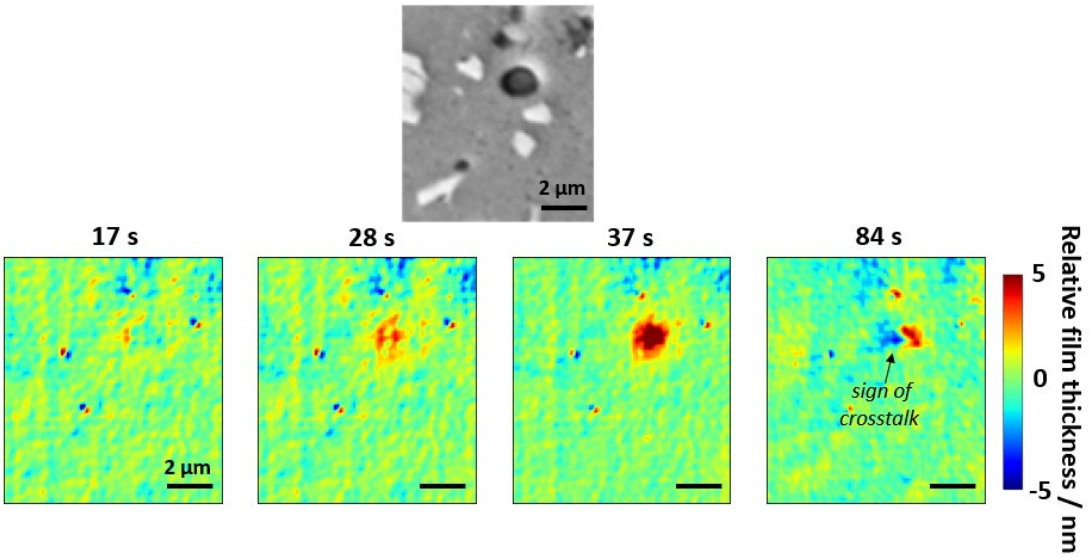

10. In contrast to other examples, herein the separation of dissolution/precipitation regions does not match with the particle positioning. This is very similar to the reported in the literature distribution of corrosion products around particles agglomerates on Al2024 alloy after a few hours of immersion in NaCl aqueous solutions.[12,19–21]

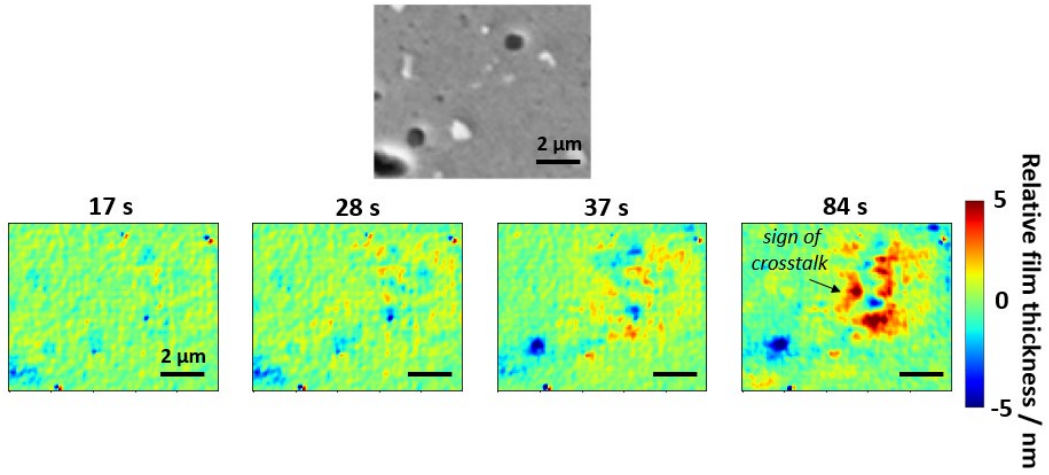

References

[1] N. Li, C. Dong, C. Man, J. Yao, *Adv Eng Mater* **2019**, *21*, 1900386.

[2] I. Olefjord, H. J. Mathieu, P. Marcus, *Surface and Interface Analysis* **1990**, *15*, 681–692.

[3] P. Cornette, S. Zanna, A. Seyeux, D. Costa, P. Marcus, *Corros Sci* **2020**, *174*, 108837.

[4] S. Chakri, A. N. Patel, I. Frateur, F. Kanoufi, E. M. M. Sutter, T. T. M. Tran, B. Tribollet, V. Vivier, *Anal Chem* **2017**, *89*, 5303–5310.

[5] S. Munteanu, J. P. Roger, Y. Fedala, F. Amiot, C. Combellas, G. Tessier, F. Kanoufi, *Faraday Discuss* **2013**, *164*, 241–258.

[6] L. Godeffroy, I. Aguilar, J. Médard, D. Larcher, J. M. Tarascon, F. Kanoufi, *Adv Energy Mater* **2022**, *12*, 2200722.

[7] https://refractiveindex.info/

[8] Mastersizer 2000, *Sample Dispersion and Refractive Index Guide. Reference Manual.*, UK, **2007**.

[9] I. Puigdomenech, "Chemical Equilibrium Diagrams," can be found under https://sites.google.com/site/chemdiagr/home, **2015**.

[10] L. Godeffroy, J.-F. Lemineur, V. Shkirskiy, M. M. Vieira, J.-M. Noël, F. Kanoufi, L. Godeffroy, J.-F. Lemineur, V. Shkirskiy, M. Miranda Vieira, J.-M. Noël, F. Kanoufi, *Small Methods* **2022**, 2200659.

[11] Y. Zhu, K. Sun, G. S. Frankel, *J Electrochem Soc* **2018**, *165*, C807–C820.

[12] P. J. Denissen, A. M. Homborg, S. J. Garcia, *J Electrochem Soc* **2019**, *166*, C3275–C3283.

[13] A. Boag, A. E. Hughes, A. M. Glenn, T. H. Muster, D. McCulloch, *Corros Sci* **2011**, *53*, 17–26.

[14] D. Veys-Renaux, N. Chahboun, E. Rocca, *Electrochim Acta* **2016**, *211*, 1056–1065.

[15] N. Birbilis, R. G. Buchheit, *J Electrochem Soc* **2005**, *152*, B140.

[16] S. K. Kairy, N. Birbilis, *Corrosion* **2020**, *76*, 464–475.

[17] N. L., X. Zhou, N. Birbilis, A. E. Hughes, J. M. C. Mol, S. J., X. Zhou, G. E., *Aluminium Alloys - New Trends in Fabrication and Applications* **2012**, DOI 10.5772/53752.

[18] M. Li, Z. Shi, X. Wu, H. Wang, Y. Liu, *Materials 2019, Vol. 12, Page 172* **2019**, *12*, 172.

[19] A. Hughes, T. H. Muster, A. Boag, A. M. Glenn, C. Luo, X. Zhou, G. E. Thompson, D. McCulloch, *Corros Sci* **2010**, *52*, 665–668.

[20] A. E. Hughes, A. Boag, A. M. Glenn, D. McCulloch, T. H. Muster, C. Ryan, C. Luo, X. Zhou, G. E. Thompson, *Corros Sci* **2011**, *53*, 27–39.

[21] P. J. Denissen, S. J. Garcia, *Electrochim Acta* **2019**, *293*, 514–524.

[22] M. Mokaddem, P. Volovitch, F. Rechou, R. Oltra, K. Ogle, *Electrochim Acta* **2010**, *55*, 3779–3786.

[23] M. A. Jakab, D. A. Little, J. R. Scully, *J Electrochem Soc* **2005**, *152*, B311.

[24] R. G. Buchheit, *J Electrochem Soc* **1995**, *142*, 3994–3996.

[25] L. Liu, Y. Xu, Y. Zhu, X. Wang, Y. Huang, *J Electrochem Soc* **2020**, *167*, 141510.

[26] S. Thomas, I. S. Cole, M. Sridhar, N. Birbilis, *Electrochim Acta* **2013**, *97*, 192–201.

[27] J. D. Yoo, K. Ogle, P. Volovitch, *Corros Sci* **2014**, *83*, 32–37.